

Detection and Astrometry of the Ba–Bb Subsystem in α Piscium: First Dual-Field Interferometry at the CHARA Array

NARSIREDDY ANUGU,¹ ROBERT KLEMENT,^{2,3,1} JOHN D. MONNIER,⁴ DOUGLAS R. GIES,⁵ GAIL H. SCHAEFER,¹ STEFAN KRAUS,⁶ SEBASTIÁN CARRAZCO-GAXIOLA,⁵ AKSHAT S. CHATURVEDI,⁵ MAYRA GUTIERREZ,⁴ BECKY FLORES,⁵ JEREMY JONES,⁵ COLIN KANE,⁵ RAINER KÖHLER,¹ KAROLINA KUBIAK,¹ OLLI W. MAJONEN,¹ NICHOLAS J. SCOTT,¹ AND KAYVON SHARIFI⁵

¹The CHARA Array of Georgia State University, Mount Wilson Observatory, Mount Wilson, CA 91023, USA

²European Organisation for Astronomical Research in the Southern Hemisphere (ESO) Casilla 19001, Santiago 19, Chile

³Université Côte d’Azur, Observatoire de la Côte d’Azur, CNRS, Boulevard de l’Observatoire, CS 34229, 06304 Nice Cedex 4, France

⁴Department of Astronomy, University of Michigan, Ann Arbor, MI 48109, USA

⁵Center for High Angular Resolution Astronomy and Department of Physics and Astronomy, Georgia State University, P.O. Box 5060, Atlanta, GA 30302-5060, USA

⁶Astrophysics Group, Department of Physics & Astronomy, University of Exeter, Stocker Road, Exeter, EX4 4QL, UK

ABSTRACT

We present the first on-sky demonstration of dual-field interferometry at the CHARA Array and the first direct resolution of the inner Ba–Bb subsystem in the bright hierarchical triple α Piscium. Using H -band fringe tracking on component A with MIRC-X to stabilize K -band science fringes on component B with MYSTIC, we detected a companion at a projected separation of 7 mas, confirming a long-suspected but previously unresolved short-period subsystem within the B component. The nearly equal H/K -band flux ratio indicates that Ba and Bb are near-twin F-type stars, consistent with the two narrow-lined components seen in optical spectra of B. By combining CHARA interferometry with archival VLTI/GRAVITY astrometry and radial velocities from archival and new spectroscopy (NARVAL and ARCEN), we derive a well-constrained orbit with a period of $P = 25$ d, eccentricity $e \simeq 0.6$, and inclination $i \simeq 65^\circ$, yielding precise dynamical masses of $1.668 \pm 0.033 M_\odot$ and $1.646 \pm 0.029 M_\odot$. No additional companion is detected down to $\Delta H \approx 5$ at separations of 0.2–2 AU. We also obtained dual-field differential astrometry of the wide A–B pair with a precision of ~ 0.234 mas at a separation of $1.85''$, with an error budget dominated by internal delay-line actuators, fringe-tracking performance and chromatic dispersion. While the long-period outer orbit is not refined by these measurements, their agreement with the published astrometric orbit provides an on-sky validation of the CHARA dual-field mode. These results establish α Psc as a well-characterized hierarchical system suitable for future benchmark studies and demonstrate CHARA’s new capability for off-axis interferometry and sub-mas astrometry on arcsecond-scale binaries.

Keywords: Long baseline interferometers (931) – High angular resolution (2167) – Interferometric binary stars (806) – Binary stars (154) – Chemically peculiar stars (226)

1. INTRODUCTION

Hierarchical multiple systems provide critical constraints on stellar evolution, angular-momentum transport, and the dynamical pathways that produce short-period binaries among intermediate-mass stars (A. Tokovinin 2014; M. Moe & R. Di Stefano 2017). Among these, short-period A-star binaries embedded within wider triples often exhibit conditions—reduced large-scale mixing, intermittent tidal interaction, and stable radiative envelopes—that can favor the development or persistence of chemical peculiarities in some components (G. W. Preston 1974; H. A. Abt & N. I. Morrell 1995; M. Netopil et al. 2017). Not all hierarchical systems host chemically peculiar (Ap and Am) stars, but their

architectures provide a useful framework for interpreting rotational, magnetic, and spectroscopic variability in systems where Ap signatures are present (Z. Mikulášek et al. 2011).

The bright, nearby (50 ± 2 pc; C. A. L. Bailer-Jones et al. 2018) visual binary system α Psc (HIP 9487) illustrates both magnetic and metallic-line chemical peculiarity, with component A (HD 12447) classified as an Ap (chemically peculiar 2) star and component B (HD 12446) as an Am (chemically peculiar 1) star (R. O. Gray & R. F. Garrison 1989). This system is among the longest-monitored visual binaries, with astrometric measurements dating back to 1779 (O. J. Lee 1913; B. D. Mason et al. 2001). Component A exhibits established

chemical peculiarities and rapid rotation, with a 1.5 d magnetic modulation detected in photometry and radio observations (K. T. Wraight et al. 2012; B. Das et al. 2022). Component B, by contrast, shows very sharp spectral lines and has long been suspected to host an equal-brightness SB2 subsystem (H. A. Abt & S. G. Levy 1985), though no spectroscopic orbit or astrometric confirmation has previously been obtained.

Because the primary goal of this project was to commission and validate the new observing mode at the Georgia State University Center for High Angular Resolution Astronomy (CHARA) Array (T. A. ten Brummelaar et al. 2005), we selected the bright ($H \sim 3.6$ mag) and well separated α Psc A–B system for an on-sky demonstration. Its wide separation, and almost equal flux double stars, make it an ideal system for testing fringe tracking, dual-channel fiber injection, and differential-delay control prior to observations of fainter science targets. Because a dual-field capability has long been a missing step in CHARA’s evolution, α Psc offered a rare opportunity: a bright, well-understood system in which we could both commission the technique and potentially uncover unresolved structure.

In this paper we report dual-field interferometric observations at CHARA (see Figure 1) and use them to (1) directly resolve the previously unseen Ba–Bb subsystem at a separation of ~ 7 mas (see Figure 2) and (2) measure the A–B separation via differential delay, providing an on-sky validation of the new astrometric mode (see Figure 3). This newly resolved subsystem clarifies the spectroscopic complexity of the B component and establishes α Psc as a well-characterized system for studying hierarchical dynamics in intermediate-mass stellar systems.

The paper is organized as follows. Section 2 describes the observational setup and data reduction. Section 3 details the discovery and orbit of the Ba–Bb subsystem using interferometric and archival spectroscopic data. Section 4 analyzes CHARA and TESS (G. R. Ricker et al. 2014) observations of component A, demonstrating rapid rotation and confirming the absence of a close companion. Section 5 presents the dual-field astrometry of the wide A–B pair. Section 6 discusses the broader astrophysical implications and future prospects of CHARA dual-field interferometry. Technical details of the dual-field implementation, astrometric error budget and validation (see Appendix A), observing log, data reduction, orbital fitting, and TESS analysis appear in the Appendices. Tables 1, and 2, summarize the α Psc system properties and the Ba–Bb orbital solutions.

2. OBSERVATIONS AND DATA REDUCTION

We observed the α Psc A–B pair on UT 2025 August 31 (MJD = 60918) and September 1 (MJD = 60919) with all six CHARA telescopes arranged in a Y-shaped configuration with baseline separations of $\mathbf{B} = 34\text{--}331$ m (T. A. ten Brummelaar et al. 2005). We im-

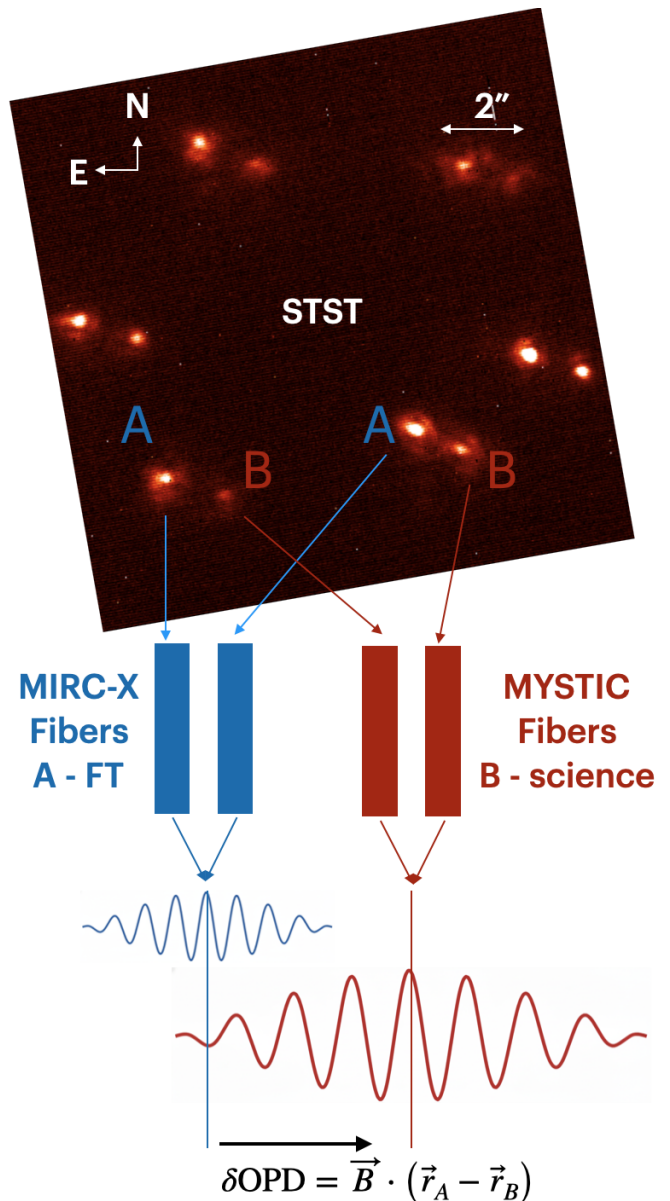


Figure 1. Light from the six 1-m CHARA telescopes is relayed to the beam-combiner laboratory and imaged on the STST (Six Telescope Star Tracker) camera with a field of view of $\sim 5''$ (N. Anugu et al. 2025). Using the STST camera coordinates of the α Psc A–B pair, flux injection into the single-mode fibers is optimized: the brighter A component into the MIRC-X H-band fibers (blue), and the fainter B component into the MYSTIC K-band fibers (red). Each fiber pair (two-telescope fringes shown for clarity) produces a corresponding white-light fringe packet, whose relative offset is set by the sky separation of the two stars. Here we define the differential optical path difference (OPD) between the two stars (and thus between the two channels) as δOPD . The measured fringe-packet separation δOPD therefore yields the instantaneous on-sky astrometric offset between the two stars with sub-mas precision. This dual-field scheme enables simultaneous fringe tracking on the bright component and long-exposure science measurements on the faint component. See detailed optical layout in Figure 4 and implementation in Appendix A.

Table 1. Basic properties of the α Psc system components.

Parameter	A	Ba	Bb
Sp. type ^a	kA0hA7SrCr	kA2hF2mF2	
d (pc) ^b	48.17 ± 0.34		
M (M_{\odot}) ^c	2.55 ± 0.11	1.668 ± 0.033	1.646 ± 0.029
P_{rot} (d) ^d	1.491 ± 0.022	—	—
R (R_{\odot}) ^e	2.33 ± 0.26	1.76 ± 0.41	1.55 ± 0.41

NOTE—^a Spectral types from R. O. Gray & R. F. Garrison (1989).

^b Distance derived from our combined astrometric and radial-velocity orbital solution (see Section 3.3).

^c Mass of component A from M. Netopil et al. (2017). Other literature estimates for component A based on position in the HRD and evolutionary tracks include $M = 2.65^{+0.21}_{-0.28} M_{\odot}$ (J. Sikora et al. 2019) and $M = 2.49 \pm 0.05 M_{\odot}$ (M. E. Shultz et al. 2022). Masses of Ba and Bb are derived from our combined orbital solution (see Section 3.3).

^d Our TESS analysis measured rotational period of component A matches with previous studies of magnetic field variability and radio bursts (E. F. Borra & J. D. Landstreet 1980; J. Sikora et al. 2019; B. Das et al. 2022).

^e Stellar radii derived from limb-darkened angular diameters from our CHARA interferometry, converted to absolute measurements using the distance from the orbital solution (see Section C).

plemented the dual-field observations leveraging both the Michigan InfraRed Combiner-eXeter (MIRC-X, 1.5–1.75 μm , N. Anugu et al. 2020a) and Michigan Young Star Imager at CHARA (MYSTIC, 2.0–2.4 μm , B. R. Setterholm et al. 2023) beam combiners. They provided angular resolution of approximately $\lambda/2B$, corresponding to spatial resolution down to ~ 0.5 and ~ 0.6 mas in the H and K bands.

We observed the α Psc A–B pair in four complementary dual-field configurations to validate repeatability and verify that the astrometric solution was independent of the choice of science combiner. Figure 1 shows the optical layout (see also Figure 4); full technical details of the dual-field concept and implementation are provided in Appendix A. First, we injected α Psc A into MIRC-X and B into MYSTIC, acquired data with MIRC-X as the group delay fringe tracking channel and MYSTIC as the science channel, and then reversed the roles so that MYSTIC served as the fringe tracker and MIRC-X as the science combiner. We then repeated the full sequence after swapping the fiber injections—injecting A into MYSTIC and B into MIRC-X—again taking data in both fringe tracker/science configurations. This four-configuration strategy provided two independent

H-band and two independent K-band astrometric solutions, enabling robust internal consistency checks for the dual-field measurements 4). Astrometry between the A–B pair followed the dual-field delay relation (Eq. A1). Full observing details (fiber injection strategy, calibrations, spectral setup) are compiled in Appendix B.

A full description of the reduction, calibration, and model fitting is provided in Appendix B. We used the public MIRC-X pipeline (N. Anugu et al. 2020a), version 1.5.0 to reduce raw data and derive 15 squared visibilities (V^2) and 10 independent closure phases (of 20 measured) for each wavelength band H and K.

3. DISCOVERY OF THE INNER BA–BB SUBSYSTEM AND ITS ORBIT

3.1. MIRC-X and MYSTIC data

The Ba–Bb subsystem was first discovered unexpectedly: during the commissioning run, the science-channel “waterfall” plot and power spectrum in both MIRC-X and MYSTIC instruments displayed an additional fringe signature (see Figure 5) inconsistent with the wide A–B geometry. A follow-up observation obtained on the subsequent night confirmed the presence of a rapidly moving companion in component B, exhibiting a change in position angle of approximately 2.2° over a one-night interval. We thus applied PMOIRE (A. Mérand 2022) algorithms for companion search to the B-component data (see Appendix C). The newly discovered Ba–Bb binary was found to have an angular separation of ~ 7 mas both bands, and H/K flux ratios compatible with equally bright components. Table 1 shows the derived properties, and Table 5 lists the measured astrometric positions and flux ratios.

This surprising result prompted us to re-examine all available complementary datasets such as archival spectroscopy and spectropolarimetry, and it became clear why the subsystem had escaped earlier spectroscopic detection: bright visual binaries are usually excluded from high-precision RV survey datasets. We also searched for additional archival interferometric data and found a usable dataset from the VLTI/GRAVITY dual-field calibration program (see below).

3.2. Archival GRAVITY calibration data

There are three GRAVITY (GRAVITY Collaboration et al. 2017) single-field snapshots of α Psc available in the ESO archive (program 112.25QQ.002). Two of these observations should have been pointed at the B component according to the data file headers. However, after careful inspection of the B-component data and comparison to the A-component snapshot, we concluded that the two B-component snapshots were inadvertently pointed at the A component, as the data present no binary signature and look almost identical to the A-component snapshot.

We searched for any additional data taken for calibration purposes, and ended up recovering a total

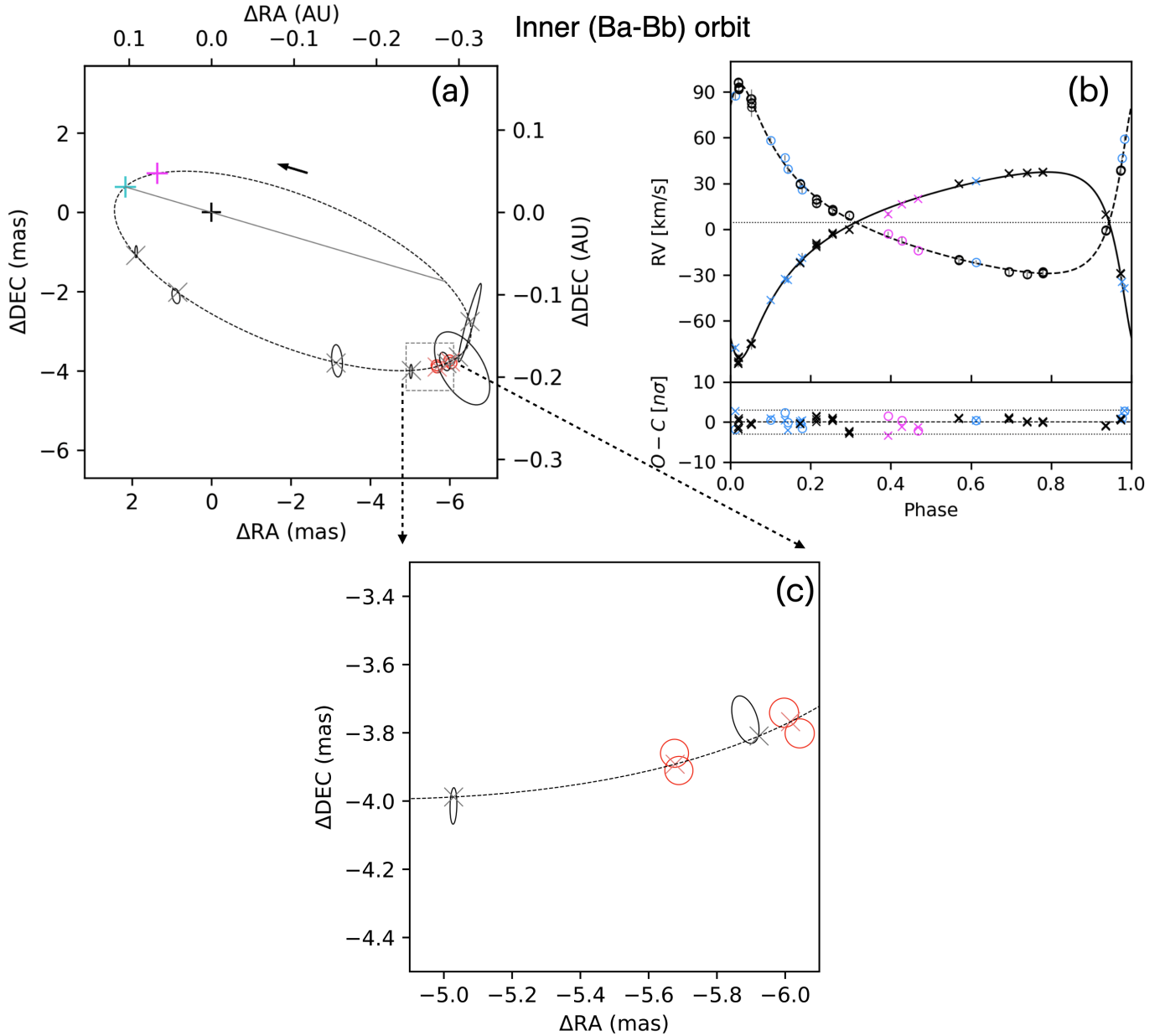


Figure 2. Astrometric and spectroscopic orbit of the inner Ba–Bb subsystem in α Psc. **(a):** Relative astrometry of Ba–Bb, with measurements denoted by 10σ error ellipses; CHARA dual-field measurements obtained in this work are shown in red, while the archival VLTI/GRAVITY measurements are shown in gray. The best-fit orbit of the Bb component is represented by the dashed curve, relative to the Ba component (“+” symbol). The positions on the best-fit orbit for the epochs of our observations are shown as “x” symbols. The magenta and cyan “+” symbols indicate the position of the periastron and the ascending node, respectively. The line of nodes is shown as a gray line. **(b):** RV curves for Ba and Bb components (solid and dashed curves, respectively), and the corresponding RV measurements (“x” symbols and open circles). The historical RVs taken from the literature are shown in blue, and our RV measurements from the archival NARVAL and newly obtained ARCEN spectra are shown in black and magenta, respectively. The horizontal line corresponds to the systemic velocity. The error bars are too small to be seen for most RVs. The lower panel shows the residuals in units of the measurement errors σ , with the dotted lines showing $\pm 3\sigma$. **(c):** Detail of the astrometric orbit showing the measurements as 3σ error ellipses.

of seven usable snapshots that were taken as part of the GRAVITY dual-field calibration program (program 60.A-9801(U)). Each of these snapshots contains data for both the A and B components taken in sequence; first, the A-component is injected into the GRAVITY fringe tracker, while the B-component goes into the GRAVITY science beam combiner, and this is followed with a swap of the components, so that the B-component becomes the fringe-tracking star, and the A-component is the science star. The data reduction, calibration, and analysis of these data is described in Appendix D. The PMOIREd analysis of these GRAVITY data resulted in seven additional astrometric points that complement and confirm the findings from CHARA/MIRC-X and MYSTIC, and it also enabled us to obtain the astrometric orbital solution (Section 3.3, Table 2).

3.3. Combined Astrometric + Spectroscopic Orbit

Radial velocities (RV) of the Ba and Bb components were measured from 56 archival spectra from the NARVAL spectropolarimetric instrument at the 2-m Telescope Bernard Lyot, and from three new spectra obtained at the ARCES spectrograph mounted on the 3.5-m telescope at the Apache Point Observatory. We also complemented our RV measurements with 10 historical RVs for both components reported by H. A. Abt et al. (1980) and H. A. Abt & S. G. Levy (1985). While those earlier studies established the system as double-lined, they did not report a unique orbital period or a full spectroscopic orbit for Ba–Bb. For details on the spectroscopic data and analysis, see Appendix D.2.

Table 2 presents the orbital parameters from the purely interferometric/astrometric fit, purely spectroscopic fit, and the final combined astrometric + spectroscopic orbital fit for the Ba–Bb subsystem. The solutions were obtained with the IDL Orbit Fitting Library⁷ (orbfit-lib; G. H. Schaefer et al. 2006, 2016). The 25 d, moderately eccentric ($e \sim 0.6$) orbit is now fully constrained, yielding precise dynamical masses of $1.668 \pm 0.033 M_{\odot}$ and $1.646 \pm 0.029 M_{\odot}$ for the two nearly equal-luminosity F-type components, as well as the dynamical parallax of 48.17 ± 0.34 pc. The Gaia EDR3-based distance to the nearby wide companion HIP 9519 at $404''.7$ separation (48.03 ± 0.08 pc; C. A. L. Bailer-Jones et al. 2021) matches our Ba–Bb dynamical distance. E. J. Shaya & R. P. Olling (2011) analyzed Hipparcos data and found that HIP 9519 is a physical C-component of the α Psc system (their Table 4, entry #132 reveals A = HIP 9487, C = HIP 9519). The Gaia distance agreement confirms this association, and the spectral classification of HIP 9519 is G1/2 V (N. Houk & C. Swift 1999). Using Ba–Bb orbital fit distance of 48.17 pc, the semimajor axis of 5.175 ± 0.018 mas corresponds to 0.2493 ± 0.0020 au.

Taken together, the wide A–B orbit and the newly constrained Ba–Bb subsystem establish α Psc as a dynamically stable hierarchical triple in which a short-period F-type inner binary and a wide tertiary companion supply the conditions expected for magnetic and chemical peculiarity in intermediate-mass stars (e.g., H. A. Abt & S. G. Levy 1985; M. Aurière et al. 2007).

Details of the orbital sampling, priors, and the incorporation of archival spectroscopic constraints are provided in Appendix E.

4. ANALYSIS OF α PSC A DATA

4.1. MIRC-X + MYSTIC data of α Psc A

Component α Psc A is partially resolved in our H band MIRC-X data, with a uniform-disk (UD) diameter of $\theta_{\text{UD}} \approx 0.45 \pm 0.05$ mas, corresponding to $2.33 \pm 0.26 R_{\odot}$ at the distance determined above. No companion is detected brighter than $\Delta H < 5$. To further confirm the result we looked at the archival data from GRAVITY and TESS. The GRAVITY data for α Psc A reveal that it is unresolved (compatible with a diameter < 0.5 mas at the VLTI baselines) and with no companion signature, confirming CHARA MIRC-X and MYSTIC results.

J. Sikora et al. (2019) estimate a radius for component A of $R_{\star} = 2.66 \pm 0.45 R_{\odot}$. For a distance of 48.17 pc, this predicts a limb-darkened angular diameter of $\theta_{\text{LD}} \simeq 9.30 R_{\star}/d \approx 0.52 \pm 0.09$ mas, consistent with our MIRC-X measurement.

4.2. TESS Photometric Variability of α Psc A

For further checking we analyzed TESS data, see Appendix F. The five available TESS sectors (4, 42, 43, 70, 97), spanning seven years, all show a clean, coherent modulation at $P = 1.490975$ d with a strong first harmonic at $P/2 \simeq 0.7455$ d (E. F. Borra & J. D. Landstreet 1980; J. Sikora et al. 2019; B. Das et al. 2022). This is consistent with α Psc A being a magnetic chemically peculiar star, as suggested by prior radio observations (B. Das et al. 2022). The phase-folded light curve shows two unequal maxima per cycle and an $\approx 2\%$ peak-to-peak modulation.

No significant power is detected at longer periods, and there is no sign of eclipses, ellipsoidal modulation, or other variability that could be associated with the newly resolved Ba–Bb subsystem.

5. ASTROMETRY AND ORBIT OF α PSC A–B

Our dual-field differential-delay measurements recover the expected separation and position angle of the wide α Psc A–B pair, yielding

$$\rho = 1850.063 \pm 0.234 \text{ mas}, \quad \text{PA} = 256.567 \pm 0.009^{\circ},$$

measured on MJD 60918 and 60919, fully consistent with the historical Washington Double Star (WDS) astrometric data (see Appendix A.4). The two nights

⁷ <https://www.chara.gsu.edu/analysis-software/orbfit-lib>

Table 2. Orbital solutions for the Ba–Bb subsystem computed with orbit-lib.

Parameter	Astrometric orbit	Spectroscopic orbit	Combined orbit
Orbital period P (d)	24.99925 ± 0.00044	24.999444 ± 0.000035	24.999428 ± 0.000033
Epoch of periastron T (MJD)	59731.09 ± 0.13	50930.707 ± 0.018	50930.714 ± 0.017
Eccentricity e	0.6143 ± 0.0051	0.5946 ± 0.0031	0.6004 ± 0.0018
Semimajor axis a (mas)	4.965 ± 0.048	—	5.175 ± 0.018
Inclination i (deg)	60.7 ± 1.3	—	65.20 ± 0.40
Longitude ascending node Ω (deg)	75.08 ± 0.63^a	—	73.08 ± 0.63
Argument of periastron ω_{Ba} (deg)	144.4 ± 1.0	139.62 ± 0.49	140.14 ± 0.42
RV semi-amplitude K_1 (km s^{-1})	—	61.02 ± 0.34	61.17 ± 0.35
RV semi-amplitude K_2 (km s^{-1})	—	61.73 ± 0.15	61.97 ± 0.47
Systemic velocity V_{sys} (km s^{-1})	—	4.45 ± 0.15	4.52 ± 0.37
Physical semimajor axis a (AU)	—	—	0.2493 ± 0.0020
Mass ratio $q = M_2/M_1$	—	—	0.9871 ± 0.0094
Total mass M_{tot} (M_{\odot})	—	—	3.315 ± 0.060
M_1 (M_{\odot})	—	—	1.668 ± 0.033
M_2 (M_{\odot})	—	—	1.646 ± 0.029
Distance d (pc)	—	—	48.17 ± 0.34

NOTE— ^a There is a 180° ambiguity in Ω when fitting purely astrometric orbits. The value listed was chosen to match Ω when constrained by RV data.

agree within uncertainty; the expected day-to-day orbital motion of the A–B pair (~ 0.04 mas day $^{-1}$) is well below our sensitivity. Total mass of the system is $M_{\text{AB}}^{\text{tot}} = 5.817 \pm 0.165$. Because the period of the outer orbit (see Figure 3) is approximately 3.3 kyr, our two CHARA epochs sample an extremely small fraction of the orbital phase. When incorporated into an updated fit of the A–B orbit (Appendix E), the CHARA points fall precisely on the Sixth Catalog of Orbits of Visual Binary Stars (hereafter ORB6⁸) trajectory and do not measurably shift any orbital element; all parameters remain consistent with published values at the $\lesssim 1\%$ level.

Thus, the present A–B astrometry should be regarded primarily as an on-sky validation of the CHARA dual-field mode—demonstrating sub-mas relative precision at $1.85''$ separation—rather than as a revision of the long-period A–B orbit.

A full error budget—including contributions from differential delay–line repeatability, baseline error, fringe-tracking residuals, and residual chromatic dispersion—is provided in Appendix A.4. These terms combine to yield a total dual-field astrometric precision of ~ 0.23 mas. This performance is at the level of the best adaptive optics (AO) based astrometric observations.

Because component B is resolved as a close Ba–Bb pair in the data, the dual-field differential delay measurement does not trace Ba or Bb individually, in two

short epochs. Rather, the measured δOPD corresponds to the flux-weighted photocenter of the B subsystem. Given that Ba and Bb have nearly equal H/K -band fluxes (within $\sim 2\%$, see Table 5), the photocenter lies within $\lesssim 0.2$ mas of the true barycenter, below our current dual-field astrometric precision (see Appendix A.5). Thus, for the purposes of the wide A–B orbit, our measurement effectively corresponds to the A–B barycentric separation.

6. DISCUSSION AND CONCLUSIONS

6.1. The Ba–Bb subsystem and system architecture

Our dual-field CHARA observations directly resolve the long-suspected Ba–Bb subsystem, establishing that component B of α Psc is itself a nearly equal-mass F-type binary with an H/K flux ratio consistent with unity. The presence of two nearly identical components also clarifies why earlier radial-velocity studies struggled to derive a coherent SB2 orbit at moderate spectral resolution.

By combining CHARA interferometry with archival VLTI/GRAVITY astrometry and spectroscopic radial velocities from NARVAL, APO/ARCES, and the literature, we derive a well-constrained orbit for Ba–Bb, with a period of $P \simeq 25$ d, eccentricity $e \simeq 0.6$, inclination $i \simeq 66^\circ$, and a physical semimajor axis of $a = 0.25$ au. The nearly equal velocity amplitudes and flux ratios imply component masses of $M_{\text{Ba}} = 1.668 \pm 0.033 M_{\odot}$ and $M_{\text{Bb}} = 1.646 \pm 0.029 M_{\odot}$, yielding a total inner-system mass of $3.315 \pm 0.060 M_{\odot}$. These values place Ba–Bb

⁸ <https://www.astro.gsu.edu/wds/orb6.html>

Outer (A-B) orbit

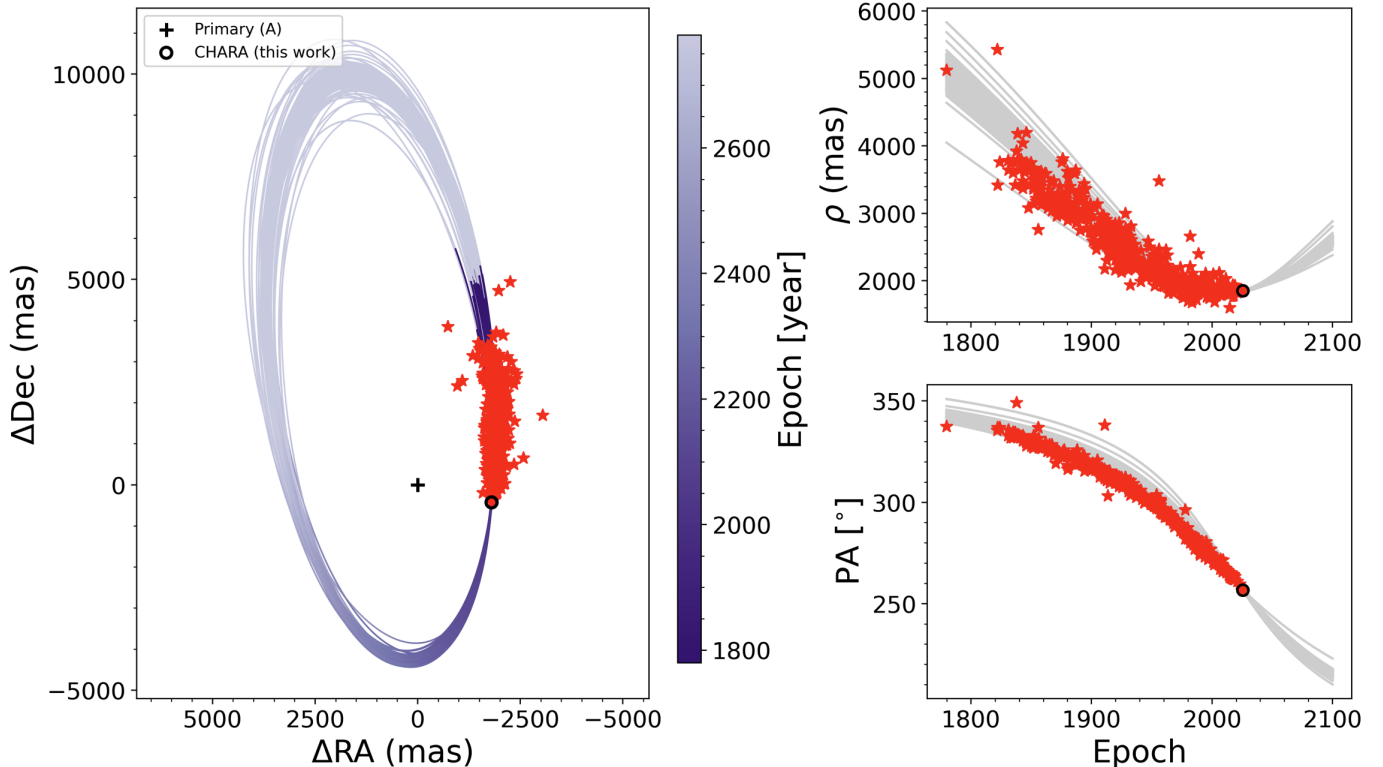


Figure 3. Orbit of the α Piscium A–B wide binary. Gray curves show 200 posterior samples from our MCMC fit to the complete Washington Double Star astrometric record (1779–2024). Red points are the historical measurements compiled in ORB6, and the two black open circles mark the new dual-field astrometric detections obtained with CHARA in 2025. North is up and East is to the left. The CHARA measurements lie exactly along the predicted orbital path at $\rho \simeq 1.85''$ and $\text{PA} \simeq 256.6^\circ$, demonstrating that the dual-field mode delivers sub-mas relative astrometry at arcsecond-level separations. Including the CHARA points does not materially change the orbital solution; all elements remain consistent with the published ORB6 orbit at the $\lesssim 1\%$ level.

in a region of the mass–period parameter space that is still underrepresented in high-precision astrometric samples: short-period (10–30 d), intermediate-mass F-type binaries that are bright and nearby enough for sub-mas astrometry remain a relatively small sample.

Although component A is a chemically peculiar, rapidly rotating star, our data do not establish a causal link between the Ba–Bb subsystem and the Ap characteristics of A. Rather, the primary contribution of this work is to provide a complete and unambiguous system architecture, which is a prerequisite for accurate atmospheric, evolutionary, and rotational modeling of all components.

The mutual orientation of the two orbital planes can be determined using the formula from F. C. Fekel (1981), and we find that their orientation is almost perpendicular ($\Phi = 80$ or 119 deg depending on the unknown factor of ± 180 deg in the longitude of the ascending node Ω_{AB} for the outer orbit). In such a configuration, the triple can experience von Zeipel–Lidov–Kozai oscillations that can cause large and cyclic variations in the inclination and eccentricity of the close binary (S. Naoz

2016). One possibility is that such long-term dynamical interactions may have contributed to the present eccentricity, although no dynamical modeling is performed here.

6.2. Dual-field astrometry at CHARA

As demonstrated in Section 5 and Appendix A.4, the wide A–B measurements primarily serve as an on-sky validation of the new CHARA dual-field mode. Because the outer orbit has a period of ~ 3.3 kyr, our two epochs do not refine the orbital elements. Nevertheless, the agreement with the ORB6 trajectory demonstrates that CHARA, in this commissioning experiment, achieves ~ 0.22 mas relative astrometric precision at a separation of $1.85''$. This level of precision is modest compared to the $\sim 25 \mu\text{as}$ differential astrometry achieved by VLTI/GRAVITY on sub-arcsecond pairs (GRAVITY Collaboration et al. 2018), but CHARA uniquely provides access to northern targets and wide ($\lesssim 5''$) separations with long baselines.

In contrast to GRAVITY, which was designed from the outset for narrow-angle astrometry with a dedicated

internal metrology system, the CHARA dual-field mode is an implementation built on existing infrastructure not originally optimized for narrow-angle dual-field astrometry. Our results therefore represent a first step that demonstrates the feasibility and scientific value of dual-field operation at CHARA, while highlighting clear paths for future instrumental upgrades.

As discussed in Appendix A.4, targeted upgrades to the internal differential delay lines (DDL) actuators, use of SPICA-FT (C. Pannetier et al. 2022) with ~ 150 nm phase tracking error and longitudinal wavelength dispersion corrections (LDC, C. Pannetier et al. 2021) are expected to reduce this floor and enable dual-field astrometry approaching the $\sim 100 \mu\text{as}$ regime.

6.3. Summary and outlook

This work presents the first dual-field interferometric observations obtained at the CHARA Array and delivers a coherent and unified picture of the α Psc system. We (i) directly resolve the B component into a ~ 7 mas inner binary, (ii) determine a short-period, eccentric Ba–Bb orbit by combining interferometry and spectroscopy, (iii) confirm that component A is a rapidly rotating, chemically peculiar star with no detected close companion, and (iv) demonstrate sub-mas dual-field astrometry on a wide binary.

Beyond the specific case of α Psc, these results mark a critical step toward extending CHARA’s sensitivity and astrometric reach to faint companions and hierarchical systems across the northern sky. A dedicated technical paper is in preparation that will quantify the end-to-end off-axis faint companion sensitivity performance, coherent integration gains, and long-exposure limits of the CHARA dual-field architecture, building on the commissioning results presented here.

ACKNOWLEDGMENTS

We thank J.-B. Le Bouquin, B. Setterholm, N. Ibrahim for their contributions to the development of the MIRC-X and MYSTIC instruments, and current and previous CHARA team members (V. Castillo, C. Farrington, R. Ligon, C. Lanthermann, H. McAlister, H. Renteria, S. Ridgway, N. Turner, T. ten Brummelaar, N. Vargas, C. Woods) for the construction and operational support of the CHARA Array. We are grateful to Dr. Rachel Matson of the US Naval Observatory who provided us with the WDS astrometric data for the A-B pair. This

work is based upon observations obtained with the Georgia State University Center for High Angular Resolution Astronomy Array at Mount Wilson Observatory. This work also makes use of VLTI/GRAVITY observations obtained under ESO programs 112.25QQ.002 and 60.A-9801(U). The CHARA Array is supported by the National Science Foundation under Grant No. AST-2034336 and AST-2407956. Institutional support has been provided from the GSU College of Arts and Sciences, Office of the Provost, and Office of the Vice President for Research and Economic Development. SK acknowledges funding for MIRC-X from the European Research Council (ERC) under the European Union’s Horizon 2020 research and innovation programme (Starting Grant No. 639889 and Consolidated Grant No. 101003096). JDM acknowledges funding for the development of MIRC-X (NASA-XRP NNX16AD43G, NSF-AST 2009489) and MYSTIC (NSF-ATI 1506540, NSF-AST 1909165). This research has made use of the Washington Double Star Catalog maintained at the U.S. Naval Observatory. This research has made use of the Jean-Marie Mariotti Center Aspro and SearchCal services. ChatGPT (GPT-5.1) was used to enhance the readability of some parts of the text.

AUTHOR CONTRIBUTIONS

NA developed the original research concept, took the CHARA observations, led the analysis, and wrote and submitted the manuscript. RK reduced the VLTI/GRAVITY observations, made the Ba–Bb orbit, and assisted with manuscript revisions. DRG, SCG, ASC, CK, and KS obtained APO RV data. DRG analyzed the archival Ba–Bb radial-velocity data and contributed to manuscript editing. GHS, JDM, SK and DRG supported the development and operation of CHARA, MIRC-X, and MYSTIC, obtained the associated funding, and contributed to manuscript writing. All authors reviewed and provided feedback on the manuscript.

Facilities: CHARA (MIRC-X & MYSTIC), VLTI(GRAVITY), ARC (APO:3.5m/ARCES), TBL (NARVAL), TESS

Software: PMOIRE (A. Mérand 2022), MIRC-X pipeline (N. Anugu et al. 2020a), lightkurve (Lightkurve Collaboration et al. 2018), JMMC OIFITS and Aspro (I. Tallon-Bosc et al. 2024), RVFIT (R. Iglesias-Marzoa et al. 2015), orbitize! package (S. Blunt et al. 2020)

APPENDIX

This Appendix provides the technical details that complement the results presented in the main paper. Appendix A describes the dual-field implementation and error budget, Appendix B summarizes the observing

setup and data reduction, Appendix C details of the interferometric data PMOIRE companion fitting, Appendix D compiles the archival interferometry and spectroscopy, Appendix E describes the orbital fitting meth-

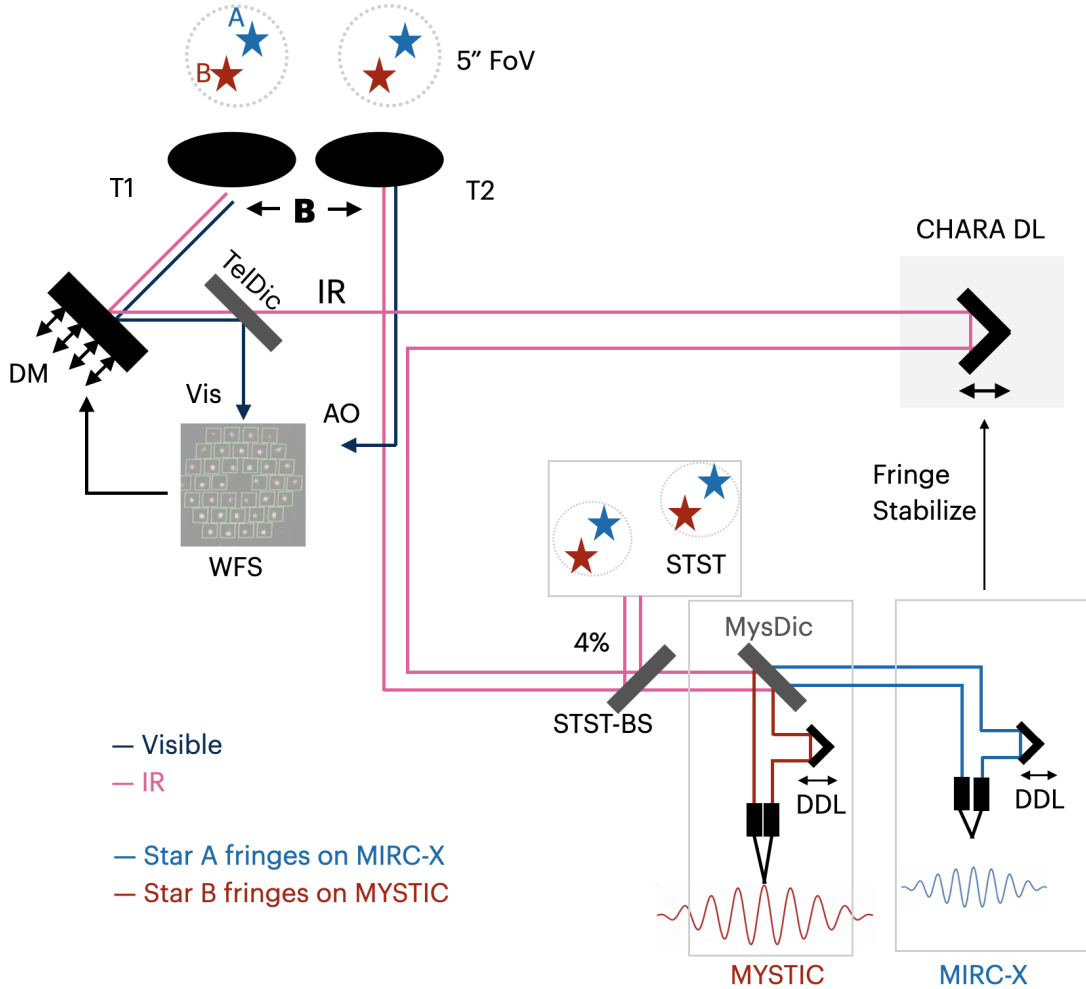


Figure 4. Schematic optical layout of the CHARA dual-field mode. For clarity we show only two telescopes and suppress the second-telescope AO/CHARA delay-line path. The $\sim 5''$ field is acquired at the telescopes; visible light feeds the AO/WFS via the telescope dichroic (TelDic), while the IR beam is relayed to the beam-combiner lab and main CHARA delay lines. The full field is imaged by STST, then a small pickoff (STST-BS) sends light to MIRC-X (H band) and MYSTIC (K band). MIRC-X fringe-tracks on component A and drives the main delay lines; MYSTIC records science fringes on component B (see Figure 5). The instrument DDLs apply the additional differential delay $B \cdot \theta$ between A and B, shifting the science beam relative to the fringe-tracking path. The fiber injection is set from the STST astrometric positions. Unlike VLTI/GRAVITY, CHARA does not have an internal metrology system; differential delays are inferred from DDL telemetry and A-B/B-A swap tests. This schematic illustrates the functional architecture rather than the full optical complexity of the six-telescope CHARA beam train.

ods, and Appendix F presents the sector-by-sector TESS photometric analysis. These materials are provided for transparency and reproducibility, while the primary scientific conclusions—the direct detection of the Ba–Bb pair and the measured day-scale orbital motion—are developed in the main text.

A. DUAL-FIELD IMPLEMENTATION AND ASTROMETRIC ERROR BUDGET

A.1. Motivation and limitations of single-field operation

Prior to this work, all CHARA beam combiners—including MIRC-X and MYSTIC—operated in single-field, on-axis mode. In this configuration a single object

supplies the flux for tip-tilt stabilization, adaptive optics correction, fringe tracking, and science beam combination. This architecture is efficient for isolated targets, but its performance degrades for binaries or faint companions located within a few arcseconds of a bright primary.

For separations $\lesssim 4''$, the tip-tilt loop becomes challenging for the fainter star: in variable seeing individual telescopes can jump to the brighter component while others remain centered on the fainter one, preventing fringe acquisition entirely. Even when the loop remains nominally stable, the single-field optical train admits flux from both stars, contaminating the science fringes with coherent leakage from the nearby star and biasing

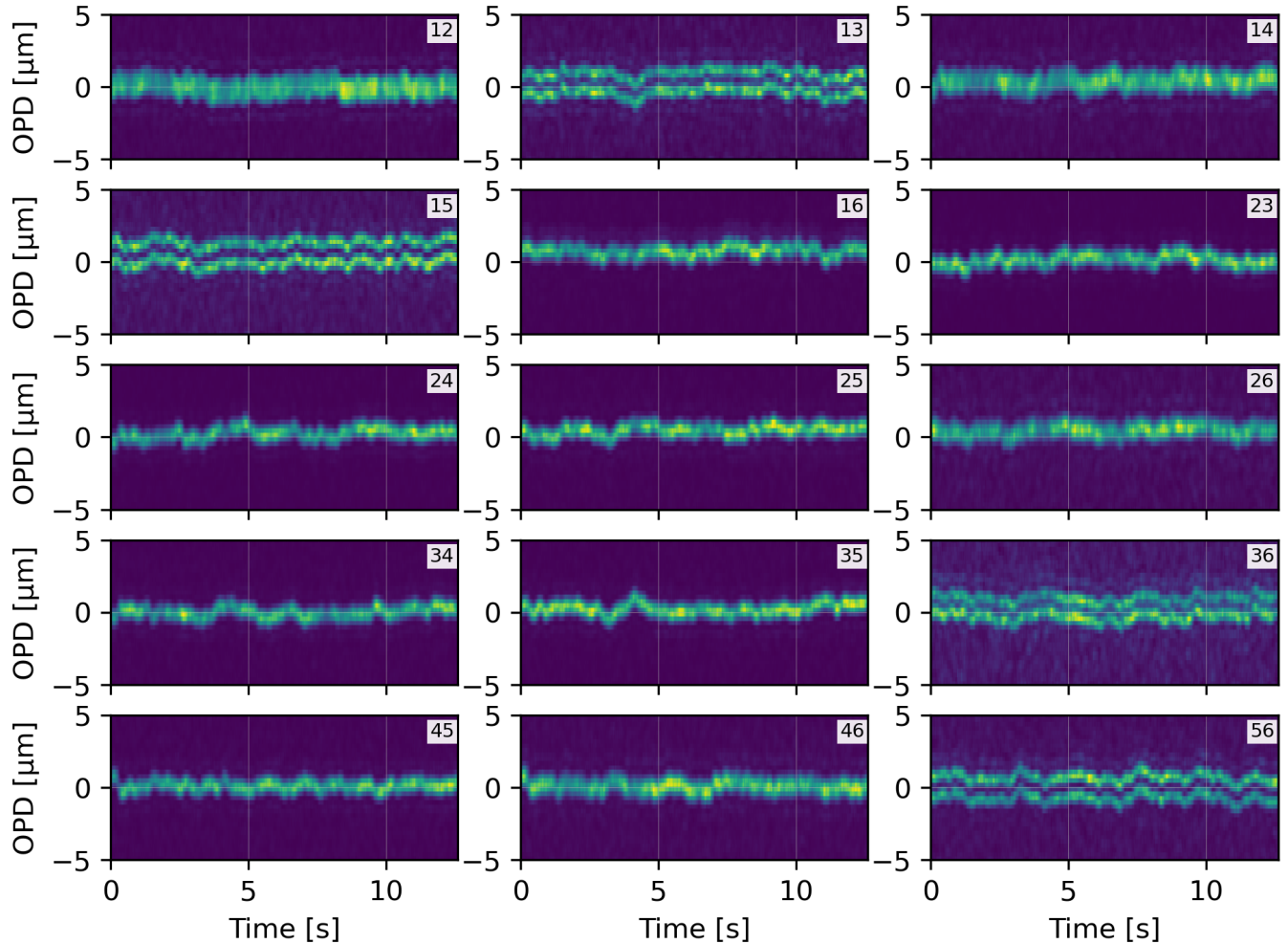


Figure 5. Waterfall plots of MYSTIC science-channel OPD residuals during dual-field observations of α Psc B (MJD = 60918). The waterfall plot shows the amplitude and position of the Fourier transform of a scan through the interferogram over time. Stable fringe packets are visible on all 15 baselines despite fringe-tracking residuals, demonstrating successful phase referencing from component A and enabling direct detection of the Ba–Bb subsystem. Each subpanel corresponds to one of the 15 baselines, labeled by the beam pair (e.g., 12 = Telescope 1–2) for the beam order E1–W2–W1–S2–S1–E2. Time increases horizontally and optical path difference (OPD) is plotted vertically; brighter lines in each waterfall window indicate higher fringe contrast and successful fringe detection. The brighter double lines in some of the large baseline waterfall windows are an indication of BaBb binary is resolved. The coherent fringe integration time for this diagnostic is 10 ms.

visibilities and closure phases. In practice this makes reliable interferometry on the faint component of a close pair difficult or impossible.

Single-field operation also limits fringe sensitivity. Because the same star must be both tracked and coherently integrated, the exposure time is restricted by the atmospheric coherence time ($\tau_0 \approx 20\text{--}40$ ms in H band) and AO corrected coherence diameter ($d_0 \approx 40\text{--}60$ cm in the near-IR). These parameters define an effective coherence volume ($\propto d_0^2 \tau_0$): once piston excursions exceed the coherence length, visibility contrast drops rapidly and the interferometric signal falls below detection thresholds (F. Eisenhauer et al. 2023). This confines CHARA sensitivity to relatively bright targets ($K \approx 8\text{--}9$ mag) and

leaves many modern science cases—long coherent integrations on faint companions or substellar objects—out of reach in single-field mode.

These limitations motivated the development of a dual-field mode at CHARA, leveraging the existing MIRC-X, MYSTIC, and STST infrastructure with only modest new observing interfaces.

A.2. Dual-field interferometry at CHARA

Dual-field off-axis interferometry addresses both classes of limitations. It separates fringe tracking and science acquisition between two stars in the field while enabling narrow-angle differential astrometry. The concept was originally outlined by M. Shao & M. M.

Colavita (1992) and has been demonstrated at PTI (M. M. Colavita et al. 1999), Keck/ASTRA (J. Woillez et al. 2014), and most recently at VLTI/GRAVITY, where dual-beam phase referencing delivers minute-long coherent integrations and microarcsecond-level astrometry (GRAVITY Collaboration et al. 2017).

Figure 4 shows that our CHARA implementation follows the same principle while exploiting the six-telescope architecture, the existing MIRC-X and MYSTIC beam combiners, and the STST acquisition camera. The internal DDLs in MIRC-X and MYSTIC provide the additional optical path required to observe two stars separated by up to $\sim 5''$ on baselines as long as 331 m. CHARA is now the only operational six-beam, dual-field near-infrared interferometer, and the only facility offering H -band fringe tracking with K -band science (and the reverse configuration).

A.3. First demonstration on the bright α Psc A–B pair

Because this commissioning run was designed primarily to demonstrate the feasibility of dual-field operation (rather than to reach the faintest possible targets), we intentionally selected the bright ($H \simeq 3.6$ mag) and well-characterized α Psc A–B system as the initial on-sky test. The A–B are within the CHARA dual-field field of view ($\sim 5''$; N. Anugu et al. 2025), while its separation is larger than the single-fiber core field of view ($\lambda/B_{\max} \lesssim 450$ mas in H and K). On such a high-flux target the MYSTIC science channel saturates before atmospheric decorrelation becomes limiting, so the effective coherence time is identical with or without phase referencing. For this demonstration, the key performance metrics are: (i) baseline length knowledge, (ii) the residual piston delivered by the MIRC-X fringe tracker, (iii) the stability and repeatability of the DDLs, and (iv) the relative wavelength calibration and chromatic dispersion between MIRC-X and MYSTIC. These elements feed directly into the differential-astrometric error budget presented in Appendix A.4.

The optical layout is summarized in Figure 1. Light from α Psc A and B is injected into independent different single-mode fibers:

- α Psc A is injected into MIRC-X (H band) and used as the real-time group-delay fringe-tracking reference. The internal diagnostic streams indicate a residual piston of 400 nm RMS on 20 ms timescales.
- α Psc B is injected into MYSTIC (K band), receiving stabilized fringes suitable for coherent averaging and model fitting of the Ba–Bb subsystem.

Fiber injection for both channels is initialized from STST astrometric positions and refined by on-sky fiber-map scans. We augmented the existing fiber-flux optimization/explorer GUI with engineering controls to support dual-field acquisition and verification.

For each projected baseline \mathbf{B} the ideal differential OPD for two stars with separation vector $\boldsymbol{\theta} = \mathbf{r}_A - \mathbf{r}_B$ is

$$\delta\text{OPD} = \mathbf{B} \cdot \boldsymbol{\theta}. \quad (\text{A1})$$

Fringe tracking on the reference star is achieved by moving the main CHARA delay lines (N. Anugu et al. 2026), which are common to both beam combiners. The off-axis science channel requires an additional differential delay equal to $\mathbf{B} \cdot \boldsymbol{\theta}$; this is provided by the instrument DDLs, which shift the science beam relative to the fringe-tracking path until the science fringes are centered (see Figure 4). We use these DDL encoder positions $\delta\text{OPD}_{\text{mech}}$ saved in the fits data headers and server logs to compute A–B astrometry.

In our instrument setup, the dominant uncertainty arises from the repeatability uncertainty of the Zaber (T-LA series, 28 mm range)-driven DDL stages, together with fringe-tracking residuals and residual chromatic dispersion. Although individual DDL moves can show repeatability error up to the $\pm 4 \mu\text{m}$ level, scan-averaging reduces the DDL repeatability term to $\sim 0.15 \mu\text{m}$. Combined in quadrature with the fringe-tracking residuals ($\sim 0.25 \mu\text{m}$) and residual chromatic dispersion ($\sim 0.2 \mu\text{m}$), the effective OPD noise is $\sim 0.36 \mu\text{m}$, corresponding to an astrometric floor of $\sim 227 \mu\text{as}$ at $1.85''$ separation. The full error budget is quantified below and summarized in Table 4.

A.4. Differential-astrometry formalism and error budget

Following the standard narrow-angle interferometry formalism (e.g., M. Shao & M. M. Colavita 1992; M. M. Colavita et al. 1999; J. Woillez et al. 2014), each projected CHARA baseline \mathbf{B}_i (15 unique baselines for six telescopes) obeys

$$\delta\text{OPD}_i = \mathbf{B}_i \cdot \boldsymbol{\theta} + \delta\text{OPD}_{\text{disp},i} + \delta\text{OPD}_{\text{inst},i}, \quad (\text{A2})$$

where $\boldsymbol{\theta}$ is the sky-plane separation vector (radians), $\delta\text{OPD}_{\text{disp},i}$ captures longitudinal dispersion (group-delay offsets between the fringe-tracking and science bands driven by air-path dispersion and effective H – K wavelength differences, C. Pannetier et al. 2021), and $\delta\text{OPD}_{\text{inst},i}$ includes residual band-to-band internal offsets. We measure five independent OPDs. W2 was used as reference. We measure OPD offsets E1W2, W1W2, S2W2, S1W2 and E2W2.

Throughout this paper, δOPD denotes a differential optical path delay; subscripts “meas”, “disp”, “inst”, and “geo” refer to the measured delay, chromatic dispersion, residual instrumental offsets, and the geometric delay computed from the (u, v) coverage, respectively. We use “mech” for the mechanical DDL stroke and “A–B”/“B–A” to label the two swap configurations.

Before fitting $\boldsymbol{\theta}$ in Eq. A2, we clean the OPDs in three steps: (i) remove the on-axis/off-axis zero-point using DDL differencing in Section A.4.1, (ii) apply

Table 3. Summary of α Psc A–B astrometry from MIRC-X and MYSTIC.

MJD	Config	ρ (mas)	PA (deg)	σ_ρ (mas)	σ_{PA} (deg)
60918.414	A-B	1850.158	256.585	0.268	0.006
60918.427	B-A	1850.004	256.622	0.283	0.010
60918.432	A-B	1849.671	256.607	0.160	0.015
60918.469	A-B	1850.200	256.587	0.206	0.007
60919.372	B-A	1850.283	256.436	0.254	0.008

NOTE—A–B/B–A are defined by the sign of the differential optical path delay: A–B corresponds to $-\delta\text{OPD}$ and B–A to $+\delta\text{OPD}$. We report ρ and PA for the same sky vector $\boldsymbol{\theta} = \mathbf{r}_A - \mathbf{r}_B$ (A relative to B; PA east of north) in all rows; therefore A–B and B–A entries are expected to agree within uncertainties and are not offset by 180° .

Table 4. Representative differential-astrometric error budget for a $1.85''$ binary on the 331 m CHARA baseline.

Error source	Budget (μas)
Baseline length ($\Delta \mathbf{B} = 10$ mm)	~ 56
DDL scan average error ($\Delta\delta\text{OPD} = 0.15$ μm)	~ 93
Fringe tracking residual (0.25 μm)	~ 156
Non-common-path OPDs between FT and SC (H - K dispersion and drifts, total 0.2 μm)	~ 125
Quadrature total	~ 227
A-B/B-A swap consistency check (systematic bound; not in quadrature)	$\lesssim 175$

NOTE— Geometric terms scale as $\delta\theta_{|\mathbf{B}|} = \theta(\Delta|\mathbf{B}|/|\mathbf{B}|)$, while OPD-related terms scale as $\delta\theta_{\text{OPD}} = \Delta(\delta\text{OPD})/|\mathbf{B}|$.

the geometric time-matching step described in Section A.4.2, and (iii) remove the static H–K dispersion via the A–B/B–A swap in Section A.4.3. The remaining baseline-dependent offsets are treated as residual chromatic/non-common-path terms.

A.4.1. Systematic-Offset Removal via On-axis–Off-axis DDL Differencing

We derive the inter-instrument OPD from the science channel by comparing MYSTIC DDL positions between two configurations while MIRC-X continues to fringe track the A component. First, we place both instruments on-axis on A and record the mechanical DDL positions (MIRC-X for fringe tracking, MYSTIC for science). Next, we keep MIRC-X on A but move MYS-

TIC off-axis to B and record the new DDL positions. The mechanical differential delay is then $\Delta\delta\text{OPD}^{\text{mech}} = \delta\text{OPD}_{\text{offaxis}}^{\text{mech}} - \delta\text{OPD}_{\text{onaxis}}^{\text{mech}}$, and the measured optical delay is $\delta\text{OPD}^{\text{meas}} = 2\Delta\delta\text{OPD}^{\text{mech}}$. This sequence removes the fixed internal zero-point common to both pointings and isolates the sky-dependent and chromatic terms. It does not remove field-dependent or time-variable aberrations (beam walk and non-common-path differences between A-B/B-A or between MIRC-X and MYSTIC), so those residuals are treated as noise terms in the OPD budget.

A.4.2. Geometric OPD time matching

As the projected baselines $\mathbf{B}_i(t)$ evolve with Earth rotation, $\delta\text{OPD}_i(t)$ changes. We therefore compute the geometric model $\delta\text{OPD}_{\text{geo}}(t) = \mathbf{B}(t) \cdot (\mathbf{r}_A - \mathbf{r}_B)$ and time-match the OPD measurements to the same model timestamps before comparing the A–B and B–A sequences for dispersion (see Figure 7).

A.4.3. A-B/B-A Swap as a Dispersion Mitigation

For H–K bands, $\delta\text{OPD}_{\text{disp}}$ is expected to reach up to 57 μm group delay for CHARA air-path differences (from Figure 6 of C. Pannetier et al. 2021). We did not use the LDC hardware in this experiment; instead, we mitigate the dispersive term by swapping which component is used for fringe tracking and which is observed in the science channel (A in MIRC-X, B in MYSTIC, then the reverse), which flips the sign of $\delta\text{OPD}_{\text{disp}}$. Any residual chromatic OPD is folded into the dispersion term in Table 4 (cf. the GRAVITY dispersion treatment in S. Lacour et al. 2014). GRAVITY explicitly tracks metrology–starlight alignment and metrology–wavelength dispersion; CHARA has no internal metrology, so those terms are not applicable here and are absorbed into the empirical OPD-noise budget.

In A-B, configuration (MIRC-X on A, MYSTIC on B) the measured delay is

$$\delta\text{OPD}_{A-B}^{\text{meas}} = \mathbf{B} \cdot \boldsymbol{\theta} + \delta\text{OPD}_{\text{disp}} + \delta\text{OPD}_{\text{inst}} \quad (\text{A3})$$

where $\delta\text{OPD}_{\text{disp}}$ is the longitudinal H–K dispersion (air/glass group-delay mismatch between the fringe-tracking and science bands) and $\delta\text{OPD}_{\text{inst}}$ absorbs residual instrumental terms. After swapping, B-A, the stars (MIRC-X on B, MYSTIC on A) we measure

$$\delta\text{OPD}_{B-A}^{\text{meas}} = -\mathbf{B} \cdot \boldsymbol{\theta} - \delta\text{OPD}_{\text{disp}} + \delta\text{OPD}_{\text{inst}} \quad (\text{A4})$$

so both the geometric term and the dispersion term reverse sign. The A-B/B-A swap cancels the static component of the H–K dispersion, but time variability in the air path and effective wavelengths between the two sequences leaves a small residual, which we include as a dispersion-noise term in the astrometric error budget. For example, for the MJD = 60918 A–B sequence the dispersion offsets are E1W2: 35.55 μm , S2W2:

21.10 μm , S1W2: 27.38 μm , and E2W2: 22.59 μm ; these offsets are removed before astrometric fitting.

Figure 6 provides a complementary diagnostic by plotting the dispersion-corrected OPDs against the projected baseline component B_{\parallel} for the same scans; the linear relation expected from $\delta\text{OPD} = \mathbf{B} \cdot \boldsymbol{\theta}$ offers a compact visual check on sign conventions, baseline geometry, and residual scatter.

A.4.4. Astrometric OPD Fit and Bootstrap

We form $\delta\text{OPD}^{\text{meas}}$ from scan-averaged DDL positions, so the DDL repeatability term is treated as the RMS scatter about the mean (zero-mean noise) rather than as a systematic offset. Likewise, the combined fringe-tracking residuals from the fringe tracker and science combiner are characterized by the RMS of the detrended piston time series (total $\sim 0.25 \mu\text{m}$; the 10–20 nm RMS contribution from the main CHARA delay lines is included here, see N. Anugu et al. (2026)) and propagated as a noise term in the OPD uncertainty (see Figure 5).

Figure 7 shows a representative $\delta\text{OPD}^{\text{meas}}$ time series for the A–B configuration (MYSTIC on B, MJD = 60918). Each panel plots the measured $\delta\text{OPD}^{\text{meas}}$ (blue points, W2 reference) for one baseline and the geometric model $\delta\text{OPD}_{\text{geo}}(t)$ (orange line) computed from the time-varying (u, v) and the adopted A–B astrometry. Over a 5-min window the geometric term can change by $\sim 20 \mu\text{m}$, corresponding to an apparent astrometric shift of $\Delta\boldsymbol{\theta} \simeq \Delta(\delta\text{OPD})/|\mathbf{B}| \approx 0.02''$ (~ 20 mas along the projected baseline for $|\mathbf{B}| \approx 214$ m), so matching OPD and (u, v) timestamps is essential. The bootstrap fit of the time series shows that the mean over each observing window reduces the effective OPD noise to $\sim 0.37 \mu\text{m}$ (corresponding to ~ 0.234 mas). The A-B/B-A swap solutions differ by $\sim 175 \mu\text{as}$, consistent with the $\lesssim 234 \mu\text{as}$ uncertainty.

Table 3 reports five astrometric measurements from five data scans. The unweighted mean formal uncertainty is 0.234 mas, and the unweighted RMS scatter in ρ about the mean (repeatability) is 0.216 mas.

A.4.5. Uncertainty Budget

For small angles the scalar separation $\theta = |\boldsymbol{\theta}|$ satisfies

$$\theta \simeq \frac{\delta\text{OPD}}{|\mathbf{B}|}, \quad (\text{A5})$$

so perturbations in baseline length and differential delay contribute to the 1- σ error in quadrature as

$$\sigma_{\theta} \simeq \left[\left(\theta \frac{\Delta|\mathbf{B}|}{|\mathbf{B}|} \right)^2 + \left(\frac{\Delta(\delta\text{OPD})}{|\mathbf{B}|} \right)^2 \right]^{1/2}. \quad (\text{A6})$$

Longer CHARA baselines reduce the astrometric term as $\sigma_{\theta} \propto |\mathbf{B}|^{-1}$, providing a geometric advantage over

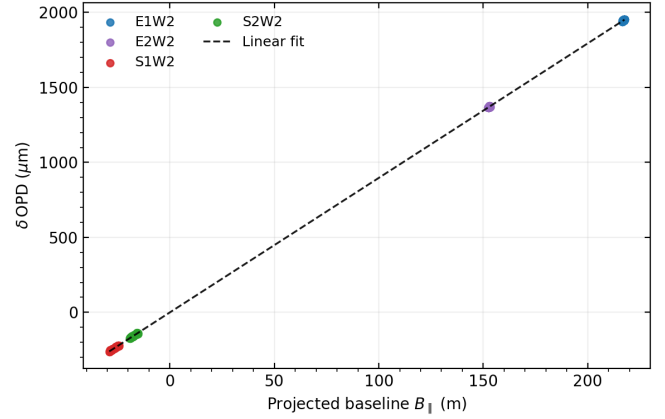


Figure 6. Dispersion-corrected $\delta\text{OPD}^{\text{meas}}$ plotted against the projected baseline component B_{\parallel} for the MJD = 60918 A–B sequence. B_{\parallel} is computed from the (u, v) coordinates via $B_{\parallel} = (u\Delta\alpha + v\Delta\delta)/|\boldsymbol{\theta}|$, where $\Delta\alpha$ and $\Delta\delta$ are the east and north components of $\boldsymbol{\theta} = \mathbf{r}_A - \mathbf{r}_B$. Each color denotes a baseline (W2 reference), and the black line is the best-fitting linear relation. For a fixed separation vector, δOPD scales linearly with B_{\parallel} (the component of the projected baseline along the A–B separation; using $|\mathbf{B}|$ would not yield a linear relation), so the alignment of the multi-baseline points provides a direct consistency check on the OPD sign conventions and time matching. The residual scatter about the fit reflects the $\sim 0.37 \mu\text{m}$ effective OPD noise used in the bootstrap uncertainty estimate.

shorter-baseline interferometric facilities for otherwise comparable error terms.

For CHARA baselines the geometric term caused by $\Delta|\mathbf{B}|$ is small compared to other terms. For example, at $\theta = 1.85''$ a typical 10 mm error observed in baseline length ($\Delta|\mathbf{B}|/|\mathbf{B}| \sim 3 \times 10^{-5}$ on 331 m) introduces only $\sim 56 \mu\text{as}$ of astrometric error. By contrast, $\Delta(\delta\text{OPD}) \sim 250$ nm gives to $\sim 156 \mu\text{as}$ at the same baseline. We verified lateral pupil shift stability using laboratory AO Shack–Hartmann data (e.g., N. Anugu et al. 2020b), and the pupil images remain stable to within $\sim 1\%$ over the observing sequence.

Table 4 summarizes the dominant contributions for the α Psc A–B measurement. The quadrature sum yields a total differential-astrometric uncertainty of $\sim 227 \mu\text{as}$ at a separation of $1.85''$. CHARA does not currently include an end-to-end laser metrology system analogous to GRAVITY, so non-common-path offsets are not measured directly and must instead be bounded empirically.

In future, the dispersion systematics could be reduced by using phase tracking available with SPICA-FT (C. Pannetier et al. 2022) and enabling the CHARA Longitudinal Dispersion Corrector (LDC) hardware correction (C. Pannetier et al. 2021), increasing the cadence of A-B/B-A and FT/Science swaps to track time-variable

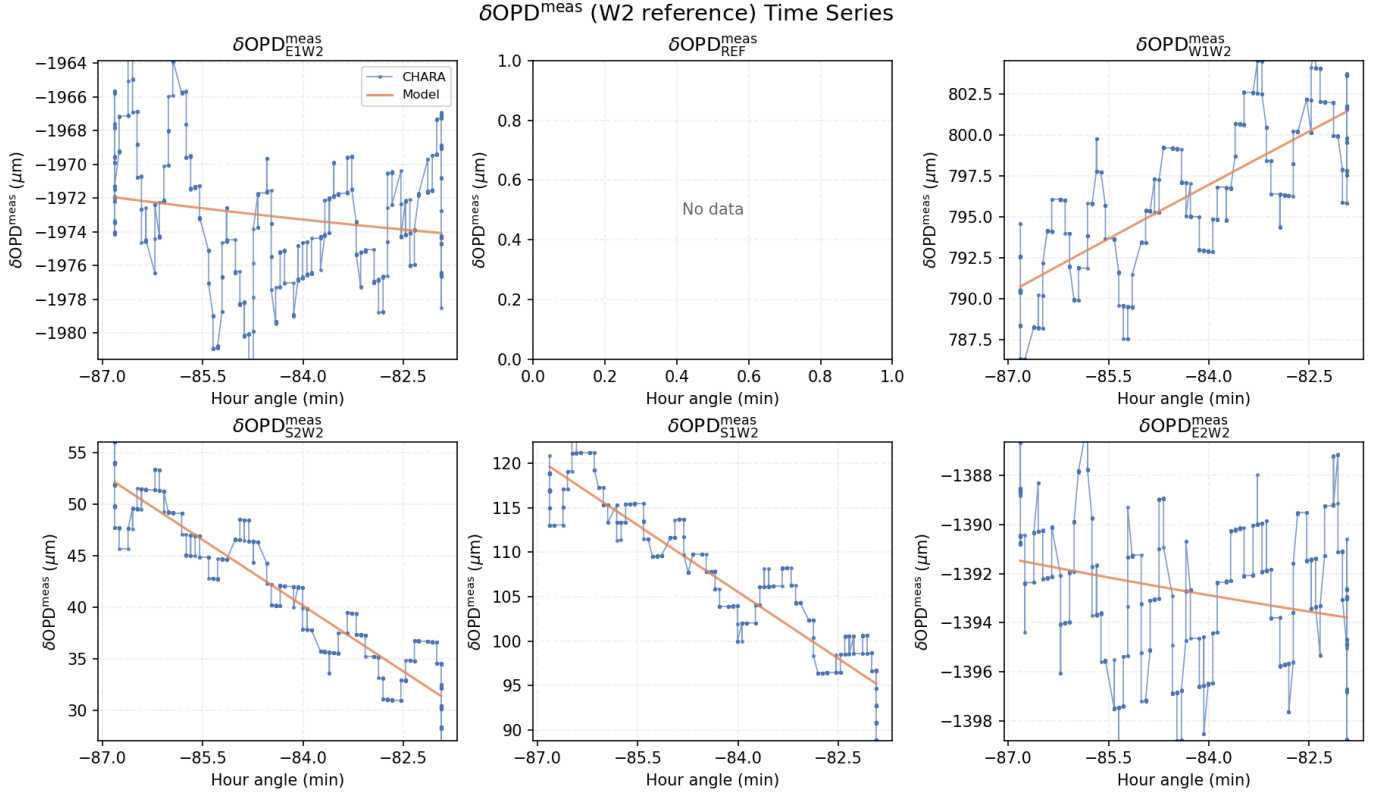


Figure 7. Representative dispersion corrected $\delta\text{OPD}^{\text{meas}}$ time series for the A–B configuration on MJD = 60918 with A in MIRC-X and B in MYSTIC (MYSTIC DDLs shown). Blue points show the measured $\delta\text{OPD}^{\text{meas}}$ (W2 reference) for the six baselines; the orange lines show the geometric model $\delta\text{OPD}_{\text{geo}}(t) = \mathbf{B}(t) \cdot (\mathbf{r}_A - \mathbf{r}_B)$ computed from the time-varying (u, v) and the A–B astrometry. The slow drift follows the changing projected baseline with hour angle, while baseline-dependent offsets between data and model indicate residual H–K dispersion and non-common-path terms. Per-scan scatter is at the 3–4 μm level, but our astrometric OPD uses time-averaged DDL positions and fringe tracking residuals, reducing the effective noise to $\sim 0.37 \mu\text{m}$.

chromatic terms, along with upgraded DDL hardware to improve repeatability and speed.

While this A–B astrometric precision is modest compared to the best achieved $\sim 25 \mu\text{as}$ achieved by VLTI/GRAVITY (GRAVITY Collaboration et al. 2018), the CHARA dual-field mode provides access to northern targets and separations up to $\sim 5''$, offering complementary astrometric reach.

A.5. Impact of Ba–Bb on the A–B astrometry

The $\sim 0.23 \text{ mas}$ precision achieved here sets the scale for what dual-field measurements can reveal about the inner Ba–Bb pair versus the wide A–B orbit. The Ba–Bb separation is only $\sim 7 \text{ mas}$; on a 331 m baseline this corresponds to a geometric differential delay of $\delta\text{OPD} \approx 11 \mu\text{m}$. For a modest Ba–Bb flux asymmetry ($\lesssim 1\%$) the resulting photocenter shift is $< 0.1 \mu\text{m}$, i.e. $\lesssim 68 \mu\text{as}$, well below our current $\sim 0.23 \text{ mas}$ dual-field precision. Related astrometric wobble measurements in intermediate-mass binaries are discussed by T. Gardner et al. (2021, 2022). Operationally, the A–B delay therefore traces the Ba–Bb barycenter rather than an individual component. This is consistent with the com-

bined Ba–Bb fringe packets seen in the science-channel OPD waterfall plots (Figure 5).

In principle, repeated dual-field astrometry over many Ba–Bb orbits could detect the photocenter wobble of the inner pair, but the expected semi-amplitude ($A_{\text{wob}} \lesssim 0.1\text{--}0.2 \text{ mas}$ for near-twin components) is comparable to the present error floor. With only two commissioning epochs the Ba–Bb signal is degenerate with differential-delay systematics and cannot be isolated from the long A–B motion. In practice, the inner orbit is therefore constrained almost entirely by the resolved Ba–Bb interferometry and archival radial velocities, while the dual-field A–B astrometry serves primarily to validate the new mode and confirm that the wide orbit is consistent with the ORB6 solution.

B. OBSERVING SETUP AND DATA REDUCTION

The $\alpha \text{ Psc}$ system was observed on UT 2025 August 31 (MJD = 60918) and September 01 (MJD = 60919) using all six CHARA 1-m telescopes (T. A. ten Brummelaar et al. 2005). We employed the standard low-resolution modes of each combiner, $R_{\text{spec}} = 50$ for

MIRC-X (H band) and $R_{\text{spec}} = 100$ for MYSTIC (K band).

Target Acquisition and Fiber Injection—At each CHARA telescope, the α Psc A–B field is first acquired on the acquisition and wavefront sensor cameras; then both the TT and AO loops are closed on the bright A component to ensure maximum wavefront stability. In dual-field mode the telescope delivers the full $\sim 5''$ field to the laboratory, so both stars propagate through the vacuum beam relay and the main delay lines without any on-sky separation applied upstream (see Figure 4).

Upon arrival in the beam-combiner lab, the pair is imaged by the STST acquisition camera. The field is positioned such that the midpoint of the A–B pair lies near the optical axis of STST, ensuring that neither component suffers vignetting from relay optics, dichroics, or pupil stops.

The actual separation of A and B into different interferometric channels occurs only on the MIRC-X + MYSTIC optical table (see Figure 4). The MIRC-X instrument is equipped with a 3D translation stage carrying the entrance single-mode fiber for X, Y, and focus positions. MYSTIC is equipped with a fast steering mirror that helps inject the selected target within the field into the single-mode fiber. Using the STST-derived astrometric coordinates, we move the MIRC-X fiber to the photocenter of component A (the fringe-tracking star), while the MYSTIC fiber is positioned on component B (the science target). Fine adjustments are performed with fiber-map scans to maximize coupling efficiency into both H -band (MIRC-X) and K -band (MYSTIC) single-mode fibers.

Once the fibers are centered, the main CHARA delay lines compensate geometric path differences for the A–B field as a whole, while the internal differential delay lines specific to MIRC-X and MYSTIC remove the residual δ OPD arising from the angular separation between the two stars. The resulting configuration provides stable fringe tracking on α Psc A and, coherently integrated science fringes on component B, enabling both the wide A–B astrometric measurement and the resolved detection of the Ba–Bb subsystem.

Co-phasing and Differential Delay Alignment—CHARA does not have a dedicated metrology link connecting the fringe-tracking and science beam combiners and their science interferograms to measure the internal path length between them accurately at the nm level. We co-phase the MIRC-X and MYSTIC instruments with the common light from the Six Telescope Simulator (STS) in the laboratory; once co-phased, the DDL positions of MIRC-X and MYSTIC were set to zero. For on-sky dual-field mode, the internal DDLs of the science combiner—the channel receiving α Psc B—were offset by the expected geometric delay (Eq. A1) corresponding to the A–B separation measured by the STST camera. We wrote a Python script that takes the separation, po-

sition angle, and CHARA (u, v) coverage to compute the expected OPD/DDL positions. This ensured that light from both A (fringe tracker) and B (science) arrived within the coherence window at the start of each scan.

Visibility Calibration—A single calibrator, HD 13546, with a uniform-disk diameter $\theta_{\text{UD}} = 0.6733 \pm 0.0611$ mas, was used for all observations. Model checks using PMOIREd confirmed that HD 13546 exhibits no closure-phase signature or visibility anomalies indicative of binarity. The same calibrator was observed repeatedly before and after each A–B science pointing to ensure consistent transfer-function tracking.

B.1. Data Reduction Pipeline

Raw interferometric data⁹ were processed using the standard MIRC-X reduction pipelines (N. Anugu et al. 2020a)¹⁰ to obtain uncalibrated, 15 squared visibilities (V^2) and 20 closure phases ($T3PHI$), of which 10 are independent. Because α Psc is extremely bright, the MYSTIC science channel saturates before atmospheric decoherence becomes limiting. The data presented here were reduced using 10 ms coherent integrations. Figure 5 shows fringe tracking residuals in the waterfall plots. Nonetheless, the stabilized piston delivered by MIRC-X enables coherent averaging without loss of fringe contrast, producing the clean Ba–Bb visibility oscillations shown in Figure 8. We reduced datasets with 4 ms integrations for MIRC-X. Instrumental and atmospheric transfer functions were derived from the calibrator scans using the IDL-based CHARA calibration routines, and applied uniformly to all H- and K-band data. We used a calibration script¹¹ written in IDL by J. D. Monnier to average the measurements over 2.5 minute intervals. The calibrated OIFITS files are available through the JMMC Optical Interferometry Database¹².

C. PMOIREd BINARY FITS FOR α PSC B

We conducted a systematic companion search around component B using PMOIREd¹³ (A. Mérand 2022).

The free model parameters were the relative astrometric offset of the two components, given by the angular separation (ρ) and the position angle (PA, measured from north to east), and the flux ratio $f_{\text{Bb}}/f_{\text{Ba}}$, where f represent the fluxes of the respective components. In addition, we fitted UD angular diameters of the two components when possible; in practice, this was hindered by the data quality and by the small, barely

⁹ <https://www.chara.gsu.edu/observers/database>

¹⁰ https://gitlab.chara.gsu.edu/lebouquj/mircx_pipeline,v1.5.0

¹¹ <https://www.chara.gsu.edu/tutorials/mirc-data-reduction>

¹² <https://oidb.jmmc.fr/index.html>

¹³ <https://github.com/amerand/PMOIREd.git,v1.4.0>

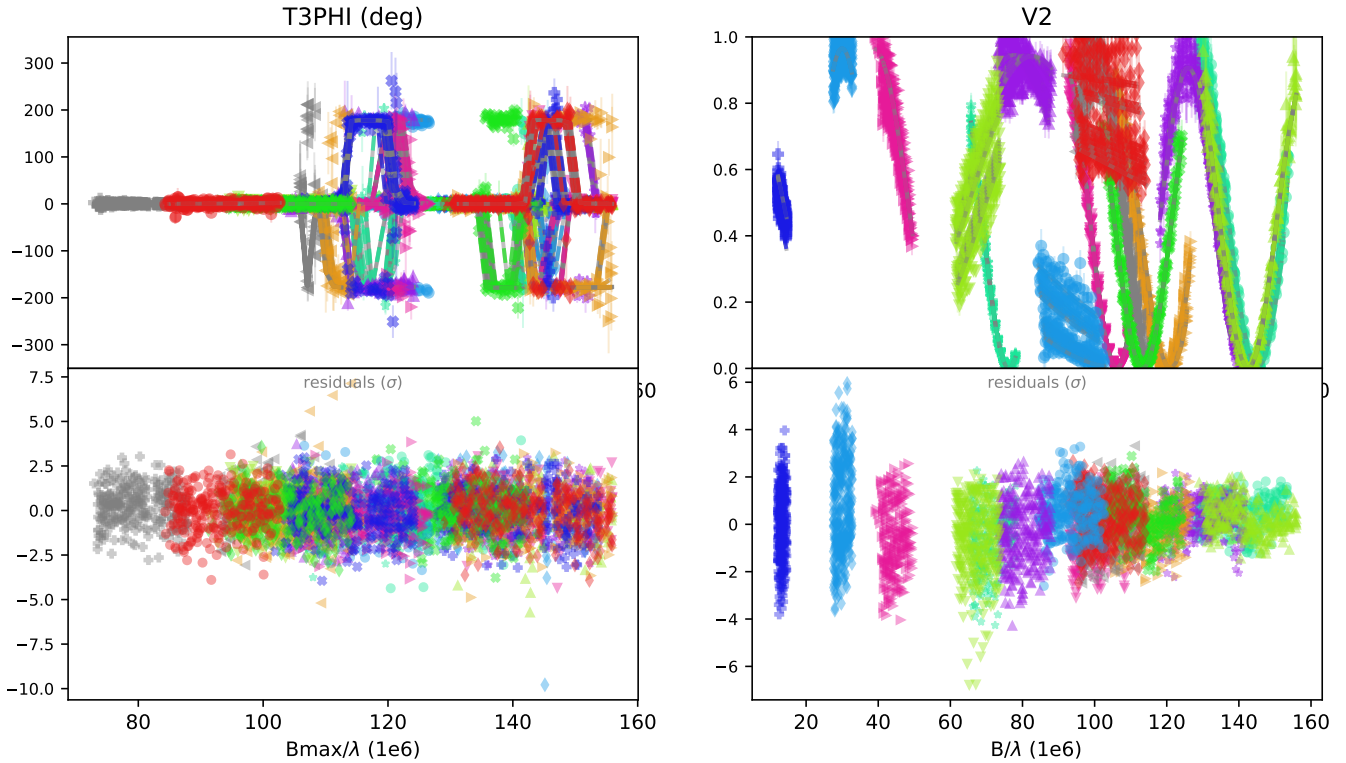


Figure 8. PMOIRED binary model fitting residuals for the first MYSTIC epoch (MJD= 60918). **Left:** Closure phase data (T3PHI, colored points) and model fit (dashed gray lines) in the upper panel, and the residuals (σ) in the lower panel. **Right:** Same for the visibility-squared data (V2) and model fit. ‘Bmax’ is the maximum projected baseline length for each telescope triangle, B is the projected baseline length for each pair of telescopes, and λ is the observed wavelength.

resolved components. An example of the data, binary fit, and the fit residuals is shown in Figure 8 for the MYSTIC data from the first epoch.

The fit to the first MIRC-X and MYSTIC epochs resulted in averaged angular diameters of $\Theta_{\text{UD},\text{Ba}} = 0.34 \pm 0.08$ mas and $\Theta_{\text{UD},\text{Bb}} = 0.30 \pm 0.08$ mas. For the second CHARA epoch, which had lower quality data, we were forced to fix $\Theta_{\text{UD},\text{Ba}}$ at 0.34 mas, while fitting only $\Theta_{\text{UD},\text{Bb}}$ in the case of MIRC-X data. For the MYSTIC data, we could not fit either diameter and therefore kept both fixed at 0.34 and 0.30 mas, respectively. As for the GRAVITY data - which, in addition to having lower angular resolution, also lack dedicated calibrators - we could not fit the diameters and kept them fixed at the same values of 0.34 and 0.30 mas, respectively.

The derived angular diameters correspond to physical stellar radii of 1.76 ± 0.41 , and 1.55 ± 0.41 , respectively, for Ba and Bb. The measured radii are compatible with the the masses inferred from our orbital solution (Table 2); using the main-sequence mass-radius relations

compiled by E. Mamajek¹⁴ (M. J. Pecaut & E. E. Mamajek 2013) leads to radii of $\sim 1.74R_{\odot}$ to $\sim 1.73R_{\odot}$ for Ba and Bb, respectively, by interpolating in the (mass, radius) entries between A9 and F0-V spectral types.

The results from the binary model fit are given in Table 5. The parameter uncertainties were refined using the bootstrap resampling algorithm implemented in PMOIRED. The fitted angular separations from MIRC-X and MYSTIC were divided by 1.0054 and 1.0067, respectively, in order to bring the CHARA instruments onto the same wavelength scale as GRAVITY (T. Gardner et al. 2022, , J. D. Monnier private comm.). For the separation uncertainties derived from the CHARA instruments, we also included an additional 0.2% error to account for the uncertainty in wavelength calibration (N. Anugu et al. 2020a; T. Gardner et al. 2022, , J. D. Monnier private comm.).

The resulting flux ratios indicate that α Psc B is an equal flux binary; averaging the individual measurements results in $f_{\text{Bb}}/f_{\text{Ba}} = 1.00 \pm 0.03$. This complicates

¹⁴ http://www.pas.rochester.edu/~emamajek/EEM_dwarf_UBVIJHK.colors_Teff.txt

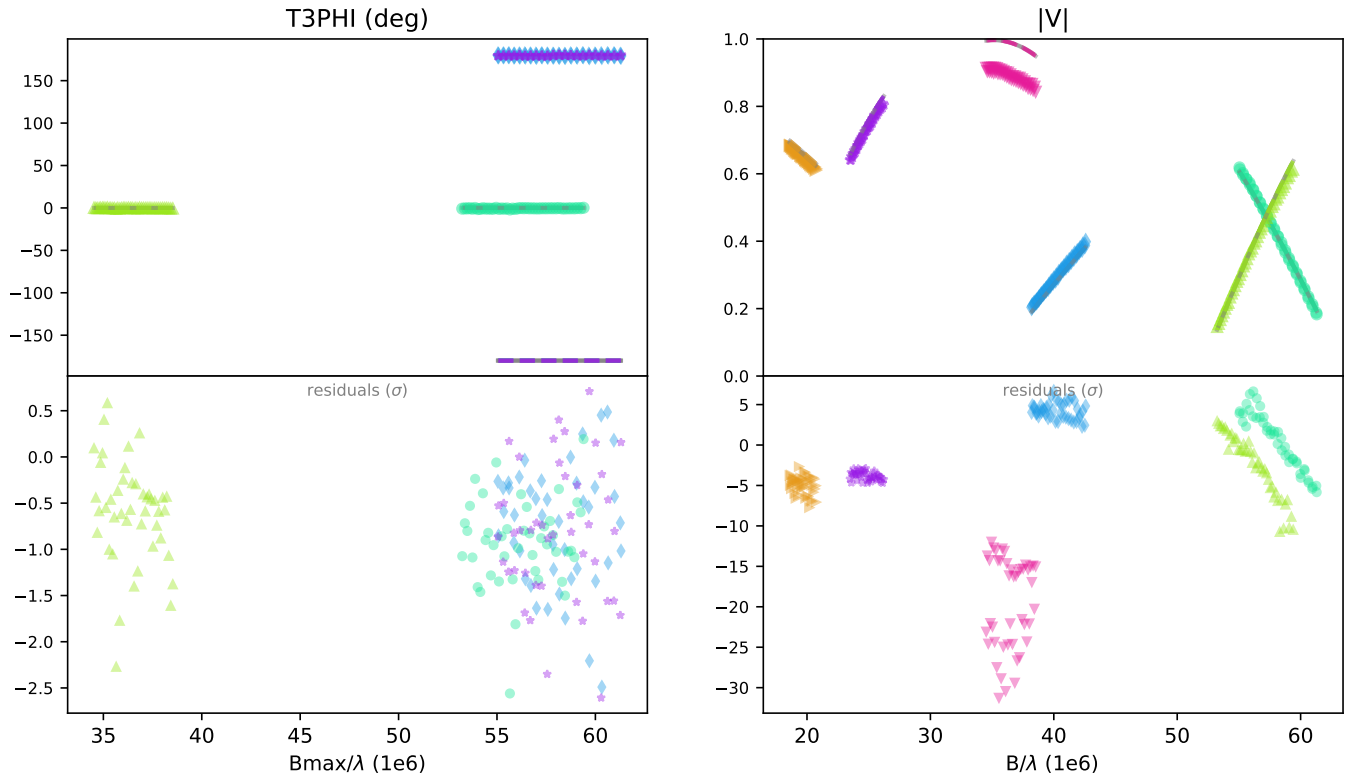


Figure 9. Same as Fig. 8, but for the GRAVITY epoch MJD = 58792, and displaying visibility ($|V|$) rather than visibility-squared. The large visibility residuals (σ) are caused by imperfect calibration due to no dedicated calibrator observations being available.

the astrometric fitting, as there is a 180° ambiguity in the fitted PA. After visual inspection of the derived positions, we thus had to flip some of the resulting PAs by 180° , so that the bulk of the positions represents realistic orbital motion. The interferometric data are therefore fully compatible with the results in Table 5 being flipped in the PAs (and the flux ratios). The final designation of which component is which rested only on assuming the Ba component has (1) the larger angular diameter in the first MIRC-X and MYSTIC epoch, and (2) the slightly lower velocity semiamplitude in the spectroscopic orbital solution.

D. ARCHIVAL INTERFEROMETRY AND SPECTROSCOPY

D.1. VLTI/GRAVITY Observations and Data Reduction

To complement the CHARA measurements, we analyzed seven archival VLTI/GRAVITY (GRAVITY Collaboration et al. 2017) dual-field observations of the α Psc A–B system obtained as part of the VLTI calibration program between 2019 and 2024. In these observations, the A-component was initially used as the phase reference star by the GRAVITY fringe tracker, while the fainter B component was injected into the science beam combiner. This was followed by rotation of the field so

that the components were swapped, and science beam combiner data were recorded on the A component, while the B component was used as the fringe tracker. The raw data were processed with the official ESO GRAVITY pipeline (version 1.7.0; V. Lapeyrere et al. 2014) in the EsoReflex environment (W. Freudling et al. 2013).

Six out of the seven observations were taken with the Auxiliary Telescopes (AT, 1.8 m diameter), with the remaining one taken with the Unit Telescopes (8 m diameter). The ATs were used in the ‘Large’ configuration corresponding to a maximum baseline length was $B_{\max} \approx 130$ m and an angular resolution of $\lambda/2B_{\max} \approx 1.3$ mas in the K band - in five out the six epochs. The data from MJD= 59894 were taken in ‘Small’ AT configuration, with $B_{\max} \approx 30$ m, and $\lambda/2B_{\max} \approx 7.5$ mas in the K band. The spectral resolution on the science beam combiner was $R \simeq 500$ (medium).

The dual-field data lack dedicated calibrator observations, preventing us from obtaining a highly reliable absolute calibration of the visibilities (while the closure phases are little affected). Since A and B components were observed in a sequence, we decided to use the data of component A, which are compatible with an unresolved point source at the VLTI baselines, as the calibrator for component B at each epoch. For the value of the A-component angular diameter used to calibrate the B-component data, we used 0.45 ± 0.05 mas deter-

Table 5. Relative positions of Bb with respect to Ba measured with GRAVITY, MIRC-X, and MYSTIC.

MJD	ρ (mas)	PA ^a (deg)	σ_a (mas)	σ_b (mas)	PA _{err} (deg)	Baselines	Instrument	$f_{\text{Bb}}/f_{\text{Ba}}$
60918.471	6.864	235.780	0.014	0.014	149.5	E1-E2-S1-S2-W2	MIRC-X	1.0198 ± 0.0040
60919.369	7.068	238.041	0.014	0.014	157.1	E1-E2-S1-S2-W2	MIRC-X	0.9754 ± 0.0024
60918.431	6.903	235.494	0.014	0.014	154.0	E1-E2-S1-S2-W1-W2	MYSTIC	0.9859 ± 0.0014
60919.388	7.139	237.824	0.014	0.014	109.3	E1-E2-S1-S2-W2	MYSTIC	0.9993 ± 0.0010
58792.153	6.434	231.397	0.018	0.003	178.7	A0-G1-J2-K0	GRAVITY	0.9979 ± 0.0010
58820.095	7.443	238.077	0.102	0.054	30.6	A0-G1-J2-J3	GRAVITY	0.99 ^b
59183.075	2.142	117.582	0.015	0.003	179.3	A0-G1-J2-K0	GRAVITY	0.9947 ± 0.0010
59834.389	2.293	157.046	0.019	0.009	12.4	A0-G1-J2-K0	GRAVITY	1.0830 ± 0.0502
59889.165	4.904	220.195	0.041	0.013	4.0	A0-G1-J2-K0	GRAVITY	0.9919 ± 0.0027
59894.127	6.983	237.408	0.024	0.012	17.8	U1-U2-U3-U4	GRAVITY	1.0056 ± 0.0053
60648.062	7.081	246.845	0.103	0.009	164.4	A0-B2-C1-D0	GRAVITY	0.9991 ± 0.0026

NOTE—PA is measured east of north. σ_a and σ_b denote the semi-major and semi-minor axes of the astrometric error ellipse, with PA_{err} giving the orientation of the semi-major axis. For the first four CHARA epochs, W1 baselines are omitted because the W1 data were not available in those scans.

^a There is 180° ambiguity in the PA due to the component having nearly equal fluxes.

^b The flux ratio fit did not converge for this epoch.

Table 6. Revised visual orbit of α Psc A–B.

Parameter	ORB6	This work
P_{AB} [yr]	3270	2822 ± 215
a_{AB} [arcsec]	7.40	7.45 ± 0.35
e_{AB}	0.465	0.4650 ± 0.0145
i_{AB} [deg]	113.4	113.01 ± 2.45
ω_{AB} [deg]	147.9	149.72 ± 5.83
Ω_{AB} [deg]	3.70	3.09 ± 6.28
$M_{\text{AB}}^{\text{tot}}$ [M_{\odot}]	...	5.817 ± 0.165

NOTE—Columns compare the ORB6 catalogue solution with our new joint fit made with `orbitize!` (S. Blunt et al. 2020). Because the wide A–B orbit lacks a radial-velocity constraint on the node, the visual solution is subject to the usual $(\omega_{\text{AB}}, \Omega_{\text{AB}}) \leftrightarrow (\omega_{\text{AB}} + 180^\circ, \Omega_{\text{AB}} + 180^\circ)$ degeneracy. Our fitted angles are expressed in the `orbitize!` convention and differ from the ORB6 values by $\simeq 180^\circ$ rotations and a swap of the argument of periastron between components, but they represent the same apparent orbit on the sky.

mined from our first MIRC-X epoch (Section 4). While this procedure led to reasonable calibration, which enabled us to use the data for the orbital fit of the Ba–Bb binary, residual systematic errors are present in the visibility data (see Fig. 9 for an example).

D.2. Radial Velocities of the Ba–Bb Subsystem

Radial velocity measurements for the Ba–Bb subsystem were assembled from a combination of historical spectroscopic observations, archival high-resolution spectropolarimetry, and new echelle spectroscopy. The system was first noted as a candidate spectroscopic binary by E. B. Frost et al. (1929), and its double-lined nature was discovered by H. A. Abt et al. (1980). Additional spectroscopic measurements by H. A. Abt & S. G. Levy (1985) confirmed that the system has two narrow-lined components of almost identical spectral line appearance and strength. Their observations were insufficient to determine an orbit or to assign the velocities to specific components. We selected the ten doubled-lined measurements from H. A. Abt et al. (1980) and H. A. Abt & S. G. Levy (1985) (made between HJD 2440846 and 2444232) for inclusion in our analysis. These appear with their assignment to components Ba and Bb in the beginning of Table 7.

The next set of measurements comes from a collection of spectra hosted at the *PolarBase*¹⁵ web site (P. Petit et al. 2014), an archive of data from the TBL/NARVAL high-resolution spectropolarimeter at the Télescope Bernard Lyot (Pic du Midi Observatory). We downloaded 56 spectra that were obtained over 14 nights (between HJD 2456906 and 2456995). These were re-binned onto a standard $\log \lambda$ wavelength grid with a

¹⁵ <https://www.polarbase.ovgso.fr>

resolving power of 20000. Significantly, these spectra record two velocity extrema separated by 50 days, which was an important clue in determining the orbital period.

Finally we obtained spectra of α Psc ourselves over the period 2025 Dec 6–8 (HJD 2461015 to 2461017) with the Apache Point Observatory 3.5-m telescope and the ARCES instrument. These observations were made under good seeing conditions so that spectra of both the A and B components were spatially resolved. ARCES covers 3500–10500 Å over 107 echelle orders with a resolving power of 30000 (S.-i. Wang et al. 2003). We reduced the spectra using standard echelle procedures in IRAF, removed the blaze function using the procedure in Appendix A of V. Kolbas et al. (2015), and then merged the orders onto a 1-dimensional $\log \lambda$ grid.

Radial velocities were measured for the NARVAL and ARCES spectra using a method that creates cross-correlation functions (CCFs) of each observed spectrum with a model composite spectrum over a range in assumed primary velocity and velocity separation (D. R. Gies & C. T. Bolton 1986; R. A. Matson et al. 2016). The model spectrum was adopted from the grid of AMBRE high resolution synthetic spectra of P. de Laverny et al. (2012) for an effective temperature of $T_{\text{eff}} = 8000$ K, gravity of $\log g = 4.0$, and solar abundances, and the spectrum was downloaded from the POLLUX¹⁶ web site. This model spectrum was adopted for both the Ba and Bb components, and a monochromatic flux ratio of 1.0 was assumed for the composite model. The wavelength range for the CCF was restricted to a region containing relatively isolated and weak metal lines in the range 4474–4578 Å (primarily from transitions of Fe I and Fe II) in order to create CCFs with minimal broadening. The derived velocities and their uncertainties are listed in Table 7. We caution that the NARVAL spectra generally also record the spectral lines of the A component, but these are broad enough that they have little impact on the measurements of the narrow-lined Ba and Bb components. We estimate that any blending issues with the A component will introduce shifts that are comparable to the uncertainty estimates for the individual radial velocities.

We initially used the orbital fitting code RVFIT (R. Iglesias-Marzoa et al. 2015) to fit the radial velocity curves of Ba–Bb and to identify those cases where the measurements were swapped between the nearly identical components. The fitted radial velocity curves are shown in the lower panel of Figure 2. The radial velocity orbits were subsequently combined with the astrometric orbit (Appendix E.1) to arrive at the physical elements reported in Table 2.

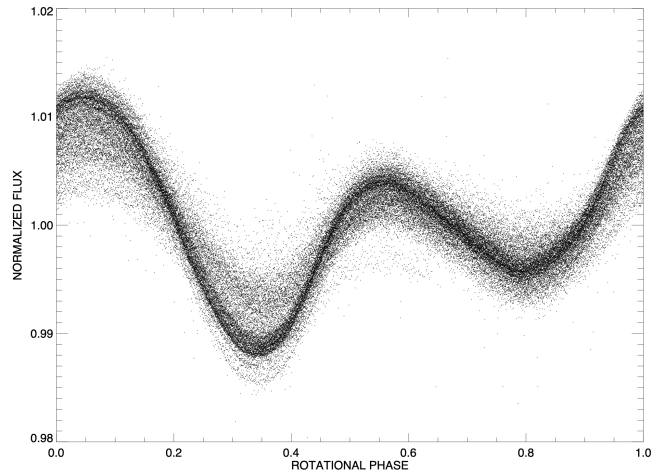


Figure 10. Phase-folded TESS light curves for α Psc at $P = 1.490975$ d. Flux is normalized to unity in each sector by dividing by the median.

E. ORBITAL FITTING METHODS

E.1. Ba–Bb orbit

We used the orbit-lib IDL library¹⁷ (orbit-lib; G. H. Schaefer et al. 2006, 2016). to fit all of the three individual solutions in Table 2. For the combined astrometric + spectroscopic solution, we scaled the measurement errors so that both the astrometric and RV datasets contribute approximately the same amount to the total residuals.

E.2. A–B orbit

We modeled the long-period α Psc A–B visual orbit using the orbitize! package (S. Blunt et al. 2020), which performs Bayesian inference of Keplerian orbits from relative astrometry. The historical measurements were extracted from the Washington Double Star Catalog (WDS) and reformatted into the orbitize! input table with separation, position angle, and their uncertainties. We adopted the combined dynamical mass ($M_A + M_B$) and parallax as Gaussian hyperparameters in the fit. Specifically, we used $M_{\text{tot}} = 5.86 \pm 0.12 M_{\odot}$ from the A+Ba+Bb masses in Table 1 and a distance prior $d = 48.17 \pm 0.34$ pc from the Ba–Bb dynamical solution, equivalent to $\varpi = 20.76 \pm 0.15$ mas.

Because the available astrometry spans only $\sim 2\%$ of the ~ 3300 yr orbit, we imposed tight Gaussian priors centered on the ORB6 solution to prevent unphysical degeneracies in $(\Omega_{AB}, \omega_{AB}, i_{AB}, a_{AB}, e_{AB})$. We used the affine-invariant MCMC sampler implemented in orbitize! with 15,000 total steps and a 5,000-step burn-in. Posterior samples were used to draw sky-plane orbits, generate separation/PA curves, and construct the corner-plot visualizations. The median posterior or-

¹⁶ <https://pollux.oreme.org>

¹⁷ <https://www.chara.gsu.edu/analysis-software/orbfit-lib>

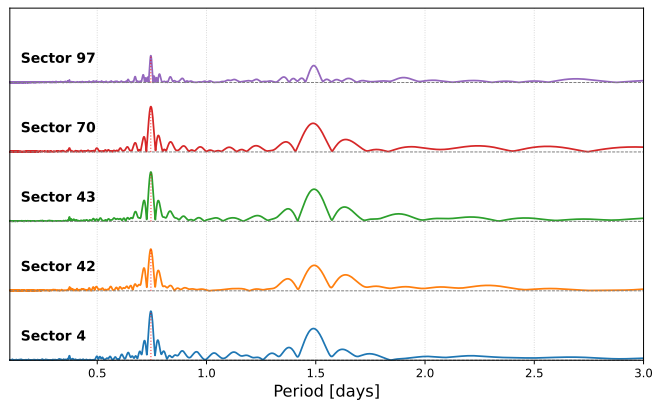


Figure 11. Sector-by-sector Lomb–Scargle periodograms for α Psc. Each curve (offset vertically for clarity) corresponds to one TESS sector. All five sectors exhibit a dominant peak at 0.7455 d, with a secondary peak at 1.490975 d. No significant power is detected at longer periods.

bit closely reproduces the ORB6 ellipse and matches all modern CCD and interferometric measurements. Table 6 presents the orbital solution.

F. TESS PHOTOMETRIC ANALYSIS: α PSC A

Here we describe the processing of the five TESS sectors used to characterize the photometric variability of the A component and its relation to the established rotation period $P_{\text{rot}} = 1.490975$ d (E. F. Borra & J. D. Landstreet 1980; J. Sikora et al. 2019; B. Das et al. 2022).

We analyzed all publicly available TESS short-cadence (120 s) observations of α Psc (HD 12447), spanning Sectors 5 (2018), 42–43 (2021), 70 (2023) and 97 (2025). Light curves were obtained via the `lightkurve` (Lightkurve Collaboration et al. 2018) interface to MAST using the `SPOC PDCSAP_FLUX` products. For each sector, we performed the following steps:

We downloaded the calibrated `PDCSAP_FLUX` time series for each TESS sector, which removes long-term instrumental trends and contamination while preserv-

ing intrinsic stellar variability. All cadences flagged by the `SPOC` quality bitmask were removed, along with residual NaNs, and each sector was median-normalized to place the light curves on a common relative-flux scale. Lomb–Scargle periodograms were then computed using the `lightkurve.periodogram` interface over 0.1–5 d with an oversampling factor of five. In every sector, the highest peak occurs at $\simeq 0.7455$ d, with a secondary peak at 1.490975 d. We treat the 0.7455 d signal as the first harmonic and adopt the established rotational period $P_{\text{rot}} = 1.490975$ d (E. F. Borra & J. D. Landstreet 1980; J. Sikora et al. 2019; B. Das et al. 2022) as a working ephemeris. Finally, the light curves were phase-folded on this period using the epoch of phase zero from B. Das et al. (2022).

The resulting summary (Figures 10 and 11) shows a stable double-wave morphology across all five sectors, despite being separated by nearly seven years of TESS operations; the harmonic structure in these figures is consistent with rotational modulation. No statistically significant power is detected at longer timescales ($P \gtrsim 3$ d). The stability of the signal across all sectors is consistent with a persistent phenomenon in component A and is unlikely to be related to the newly resolved Ba–Bb subsystem detected in our CHARA dual-field observations.

The Lomb–Scargle periodograms for all five TESS sectors show a sequence of peaks at $P_{\text{rot}}/2$ and P_{rot} , a pattern that can be produced by rotational modulation. The strongest peak occurs at $P_{\text{rot}}/2 \simeq 0.7455$ d, with a significant peak at $P_{\text{rot}} = 1.490975$ d. When folded on the full rotation period, the light curves exhibit a persistent double-wave morphology whose relative lobe amplitudes vary between sectors, consistent with evolving surface structure. The double-wave rotational light curve can arise from surface inhomogeneities related to the magnetic field.

Future high-angular-resolution observations in J band with MIRC-X and visible-wavelength (R band) observations with SPICA (D. Mourard et al. 2017) will provide both higher spatial resolution and enable direct imaging tests of the surface structure implied by the TESS light curves.

REFERENCES

- Abt, H. A., & Levy, S. G. 1985, *ApJS*, 59, 229, doi: [10.1086/191070](https://doi.org/10.1086/191070)
- Abt, H. A., & Morrell, N. I. 1995, *ApJS*, 99, 135, doi: [10.1086/192182](https://doi.org/10.1086/192182)
- Abt, H. A., Sanwal, N. B., & Levy, S. G. 1980, *ApJS*, 43, 549, doi: [10.1086/190682](https://doi.org/10.1086/190682)
- Anugu, N., Le Bouquin, J.-B., Monnier, J. D., et al. 2020a, *AJ*, 160, 158, doi: [10.3847/1538-3881/aba957](https://doi.org/10.3847/1538-3881/aba957)
- Anugu, N., ten Brummelaar, T., Turner, N. H., et al. 2020b, in *Society of Photo-Optical Instrumentation Engineers (SPIE) Conference Series*, Vol. 11446, *Optical and Infrared Interferometry and Imaging VII*, ed. P. G. Tuthill, A. Mérand, & S. Sallum, 1144622, doi: [10.1117/12.2561560](https://doi.org/10.1117/12.2561560)
- Anugu, N., Monnier, J. D., Setterholm, B. R., et al. 2025, in *Proceedings of SPIE — Astronomical Interferometry 2025*, Vol. 13627, 136270H, doi: [10.1117/12.3060177](https://doi.org/10.1117/12.3060177)

Table 7. Radial velocity measurements used in the orbit fitting. Times are heliocentric Julian dates (HJD, days).

HJD	RV ₁	σ_{RV_1}	RV ₂	σ_{RV_2}
	(km s ⁻¹)			
2440846.755	31.40	1.40	-21.60	1.40
2443055.827	-34.40	2.10	46.70	1.10
2443055.965	-38.60	2.20	59.30	1.70
2443459.776	-32.40	1.60	46.80	1.80
2443460.722	-21.10	2.00	30.30	1.30
2443808.884	-46.30	1.30	58.20	1.80
2443809.975	-33.00	1.40	39.40	3.00
2443810.853	-18.60	3.10	26.00	2.10
2443831.687	-77.40	1.60	87.50	2.50
2444232.630	-75.10	0.90	85.50	2.40
2456906.597	-83.33	1.53	92.12	1.86
2456906.599	-83.89	1.87	92.54	2.50
2456906.600	-84.20	1.81	93.41	2.50
2456906.602	-83.92	1.88	91.64	2.51
2456925.554	37.23	1.57	-28.14	1.83
2456925.556	37.31	1.52	-28.28	1.75
2456925.557	37.28	1.61	-28.38	1.81

NOTE—This Table is published in its entirety in the electronic version. A portion is shown here for guidance regarding its form and content.

Anugu, N., Turner, N. H., ten Brummelaar, T. A., et al. 2026, arXiv e-prints, arXiv:2602.16009,

doi: [10.48550/arXiv.2602.16009](https://doi.org/10.48550/arXiv.2602.16009)

Aurière, M., Wade, G. A., Silvester, J., et al. 2007, *A&A*, 475, 1053, doi: [10.1051/0004-6361:20078189](https://doi.org/10.1051/0004-6361:20078189)

Bailer-Jones, C. A. L., Rybizki, J., Fouesneau, M., Demleitner, M., & Andrae, R. 2021, *AJ*, 161, 147, doi: [10.3847/1538-3881/abd806](https://doi.org/10.3847/1538-3881/abd806)

Bailer-Jones, C. A. L., Rybizki, J., Fouesneau, M., Mantelet, G., & Andrae, R. 2018, *AJ*, 156, 58, doi: [10.3847/1538-3881/aacb21](https://doi.org/10.3847/1538-3881/aacb21)

Blunt, S., Wang, J. J., Angelo, I., et al. 2020, *AJ*, 159, 89, doi: [10.3847/1538-3881/ab6663](https://doi.org/10.3847/1538-3881/ab6663)

Borra, E. F., & Landstreet, J. D. 1980, *ApJS*, 42, 421, doi: [10.1086/190656](https://doi.org/10.1086/190656)

Colavita, M. M., Wallace, J. K., Hines, B. E., et al. 1999, *ApJ*, 510, 505, doi: [10.1086/306579](https://doi.org/10.1086/306579)

Das, B., Chandra, P., Shultz, M. E., et al. 2022, *ApJ*, 925, 125, doi: [10.3847/1538-4357/ac2576](https://doi.org/10.3847/1538-4357/ac2576)

de Laverny, P., Recio-Blanco, A., Worley, C. C., & Plez, B. 2012, *A&A*, 544, A126,

doi: [10.1051/0004-6361/201219330](https://doi.org/10.1051/0004-6361/201219330)

Eisenhauer, F., Monnier, J. D., & Pfuhl, O. 2023, *ARA&A*, 61, 237, doi: [10.1146/annurev-astro-121622-045019](https://doi.org/10.1146/annurev-astro-121622-045019)

Fekel, Jr., F. C. 1981, *ApJ*, 246, 879, doi: [10.1086/158981](https://doi.org/10.1086/158981)

Freudling, W., Romaniello, M., Bramich, D. M., et al. 2013, *A&A*, 559, A96, doi: [10.1051/0004-6361/201322494](https://doi.org/10.1051/0004-6361/201322494)

Frost, E. B., Barrett, S. B., & Struve, O. 1929, *Publications of the Yerkes Observatory*, 7, 1

Gardner, T., Monnier, J. D., Fekel, F. C., et al. 2021, *ApJ*, 921, 41, doi: [10.3847/1538-4357/ac1172](https://doi.org/10.3847/1538-4357/ac1172)

Gardner, T., Monnier, J. D., Fekel, F. C., et al. 2022, *AJ*, 164, 184, doi: [10.3847/1538-3881/ac8eae](https://doi.org/10.3847/1538-3881/ac8eae)

Gies, D. R., & Bolton, C. T. 1986, *ApJS*, 61, 419, doi: [10.1086/191118](https://doi.org/10.1086/191118)

Gravity Collaboration, Abuter, R., Accardo, M., et al. 2017, *A&A*, 602, A94, doi: [10.1051/0004-6361/201730838](https://doi.org/10.1051/0004-6361/201730838)

Gravity Collaboration, Abuter, R., Amorim, A., et al. 2018, *A&A*, 618, L10, doi: [10.1051/0004-6361/201834294](https://doi.org/10.1051/0004-6361/201834294)

Gray, R. O., & Garrison, R. F. 1989, *ApJS*, 70, 623, doi: [10.1086/191349](https://doi.org/10.1086/191349)

Houk, N., & Swift, C. 1999, *Michigan Spectral Survey*, 5, 0

Iglesias-Marzoa, R., López-Morales, M., & Jesús Arévalo Morales, M. 2015, *PASP*, 127, 567, doi: [10.1086/682056](https://doi.org/10.1086/682056)

Kolbas, V., Pavlovski, K., Southworth, J., et al. 2015, *MNRAS*, 451, 4150, doi: [10.1093/mnras/stv1261](https://doi.org/10.1093/mnras/stv1261)

Lacour, S., Eisenhauer, F., Gillessen, S., et al. 2014, *A&A*, 567, A75, doi: [10.1051/0004-6361/201423940](https://doi.org/10.1051/0004-6361/201423940)

Lapeyrere, V., Kervella, P., Lacour, S., et al. 2014, in *Society of Photo-Optical Instrumentation Engineers (SPIE) Conference Series*, Vol. 9146, *Optical and Infrared Interferometry IV*, ed. J. K. Rajagopal, M. J. Creech-Eakman, & F. Malbet, 91462D, doi: [10.1117/12.2056850](https://doi.org/10.1117/12.2056850)

Lee, O. J. 1913, *ApJ*, 38, 502, doi: [10.1086/142048](https://doi.org/10.1086/142048)

Lightkurve Collaboration, Cardoso, J. V. d. M., Hedges, C., et al. 2018, *Lightkurve: Kepler and TESS time series analysis in Python*, *Astrophysics Source Code Library*, record ascl:1812.013 <http://ascl.net/1812.013>

Mason, B. D., Wycoff, G. L., Hartkopf, W. I., Douglass, G. G., & Worley, C. E. 2001, *AJ*, 122, 3466, doi: [10.1086/323920](https://doi.org/10.1086/323920)

Matson, R. A., Gies, D. R., Guo, Z., & Orosz, J. A. 2016, *AJ*, 151, 139, doi: [10.3847/0004-6256/151/6/139](https://doi.org/10.3847/0004-6256/151/6/139)

Mérand, A. 2022, in *Society of Photo-Optical Instrumentation Engineers (SPIE) Conference Series*, Vol. 12183, *Optical and Infrared Interferometry and Imaging VIII*, ed. A. Mérand, S. Sallum, & J. Sanchez-Bermudez, 121831N, doi: [10.1117/12.2626700](https://doi.org/10.1117/12.2626700)

- Mikulášek, Z., Krtička, J., Henry, G. W., et al. 2011, *A&A*, 534, L5, doi: [10.1051/0004-6361/201117784](https://doi.org/10.1051/0004-6361/201117784)
- Moe, M., & Di Stefano, R. 2017, *The Astrophysical Journal Supplement Series*, 230, 15, doi: [10.3847/1538-4365/aa6fb6](https://doi.org/10.3847/1538-4365/aa6fb6)
- Mourard, D., Bério, P., Perraut, K., et al. 2017, *Journal of the Optical Society of America A*, 34, A37, doi: [10.1364/JOSAA.34.000A37](https://doi.org/10.1364/JOSAA.34.000A37)
- Naoz, S. 2016, *ARA&A*, 54, 441, doi: [10.1146/annurev-astro-081915-023315](https://doi.org/10.1146/annurev-astro-081915-023315)
- Netopil, M., Paunzen, E., Hümmerich, S., & Bernhard, K. 2017, *MNRAS*, 468, 2745, doi: [10.1093/mnras/stx674](https://doi.org/10.1093/mnras/stx674)
- Pannetier, C., Mourard, D., Cassaing, F., et al. 2021, *MNRAS*, 507, 1369, doi: [10.1093/mnras/stab1922](https://doi.org/10.1093/mnras/stab1922)
- Pannetier, C., Bério, P., Mourard, D., et al. 2022, in *Society of Photo-Optical Instrumentation Engineers (SPIE) Conference Series*, Vol. 12183, *Optical and Infrared Interferometry and Imaging VIII*, ed. A. Mérand, S. Sallum, & J. Sanchez-Bermudez, 1218309, doi: [10.1117/12.2628897](https://doi.org/10.1117/12.2628897)
- Pecaut, M. J., & Mamajek, E. E. 2013, *ApJS*, 208, 9, doi: [10.1088/0067-0049/208/1/9](https://doi.org/10.1088/0067-0049/208/1/9)
- Petit, P., Louge, T., Théado, S., et al. 2014, *PASP*, 126, 469, doi: [10.1086/676976](https://doi.org/10.1086/676976)
- Preston, G. W. 1974, *ARA&A*, 12, 257, doi: [10.1146/annurev.aa.12.090174.001353](https://doi.org/10.1146/annurev.aa.12.090174.001353)
- Ricker, G. R., Winn, J. N., Vanderspek, R., et al. 2014, in *Society of Photo-Optical Instrumentation Engineers (SPIE) Conference Series*, Vol. 9143, *Space Telescopes and Instrumentation 2014: Optical, Infrared, and Millimeter Wave*, ed. J. M. Oschmann, Jr., M. Clampin, G. G. Fazio, & H. A. MacEwen, 914320, doi: [10.1117/12.2063489](https://doi.org/10.1117/12.2063489)
- Schaefer, G. H., Simon, M., Beck, T. L., Nelan, E., & Prato, L. 2006, *AJ*, 132, 2618, doi: [10.1086/508935](https://doi.org/10.1086/508935)
- Schaefer, G. H., Hummel, C. A., Gies, D. R., et al. 2016, *AJ*, 152, 213, doi: [10.3847/0004-6256/152/6/213](https://doi.org/10.3847/0004-6256/152/6/213)
- Setterholm, B. R., Monnier, J. D., Le Bouquin, J.-B., et al. 2023, *Journal of Astronomical Telescopes, Instruments, and Systems*, 9, 025006, doi: [10.1117/1.JATIS.9.2.025006](https://doi.org/10.1117/1.JATIS.9.2.025006)
- Shao, M., & Colavita, M. M. 1992, *A&A*, 262, 353
- Shaya, E. J., & Olling, R. P. 2011, *ApJS*, 192, 2, doi: [10.1088/0067-0049/192/1/2](https://doi.org/10.1088/0067-0049/192/1/2)
- Shultz, M. E., Owocki, S. P., ud-Doula, A., et al. 2022, *MNRAS*, 513, 1429, doi: [10.1093/mnras/stac136](https://doi.org/10.1093/mnras/stac136)
- Sikora, J., Wade, G. A., Power, J., & Neiner, C. 2019, *MNRAS*, 483, 2300, doi: [10.1093/mnras/sty3105](https://doi.org/10.1093/mnras/sty3105)
- Tallon-Bosc, I., Berger, J.-P., Matter, A., et al. 2024, in *SF2A-2024: Proceedings of the Annual meeting of the French Society of Astronomy and Astrophysics*, ed. M. Béthermin, K. Baillié, N. Lagarde, J. Malzac, R. M. Ouazzani, J. Richard, O. Venot, & A. Siebert, 215–216
- ten Brummelaar, T. A., McAlister, H. A., Ridgway, S. T., et al. 2005, *ApJ*, 628, 453, doi: [10.1086/430729](https://doi.org/10.1086/430729)
- Tokovinin, A. 2014, *Annual Review of Astronomy and Astrophysics*, 52, 1, doi: [10.1146/annurev-astro-081913-040003](https://doi.org/10.1146/annurev-astro-081913-040003)
- Wang, S.-i., Hildebrand, R. H., Hobbs, L. M., et al. 2003, in *Society of Photo-Optical Instrumentation Engineers (SPIE) Conference Series*, Vol. 4841, *Instrument Design and Performance for Optical/Infrared Ground-based Telescopes*, ed. M. Iye & A. F. M. Moorwood, 1145–1156, doi: [10.1117/12.461447](https://doi.org/10.1117/12.461447)
- Willez, J., Wizinowich, P., Akeson, R., et al. 2014, *ApJ*, 783, 104, doi: [10.1088/0004-637X/783/2/104](https://doi.org/10.1088/0004-637X/783/2/104)
- Wraight, K. T., Fossati, L., Netopil, M., et al. 2012, *MNRAS*, 420, 757, doi: [10.1111/j.1365-2966.2011.20090.x](https://doi.org/10.1111/j.1365-2966.2011.20090.x)